Defense Technical Information Center Compilation Part Notice

ADP010760

TITLE: Aerodynamic Measurements at Low Raynolds Numbers for Fixed Wing Micro-Air Vehicles

This paper is part of the following report:

TITLE: Development and Operation of UAVs for Military and Civil Applications [Developpement et utilisation des avions sans pilote [UAV] pour des applications civiles et militaires]

The following component part numbers comprise the compilation report:

ADP010752 thru ADP010763

Aerodynamic Measurements at Low Reynolds Numbers for Fixed Wing Micro-Air Vehicles

Thomas J. Mueller
Roth-Gibson Professor
Hessert Center for Aerospace Research
Department of Aerospace and Mechanical Engineering
University of Notre Dame
Notre Dame, IN 46556
USA

Summary

A description of the micro-air vehicle (MAV) concept and design requirements is presented. These vehicles are very small and therefore operate at chord Reynolds numbers below 200,000 where very little data is available on the performance of lifting surfaces, i.e., airfoils and low aspect-ratio wings. This paper presents the results of a continuing study of the methods that can be used to obtain reliable force and moment data on thin wings in wind and water tunnels. To this end, a new platform force and moment balance, similar to an already existing balance, was designed and built to perform lift, drag and moment measurements at low Reynolds numbers. Balance characteristics and validation data are presented. Results show a good agreement between published data and data obtained with the new balance. Results for lift, drag and pitching moment about the quarter chord with the existing aerodynamic balance on a series of thin flat plates and cambered plates at low Reynolds numbers are presented. They show that the cambered plates offer better aerodynamic characteristics and performance. Moreover, it appears that the trailing-edge geometry of the wings and the turbulence intensity up to about 1% in the wind tunnel do not have a strong effect on the lift and drag for thin wings at low Reynolds numbers. However, the presence of two endplates for two-dimensional tests and one endplate for the semi-infinite tests appears to have an undesirable influence on the lift characteristics at low Reynolds numbers. The drag characteristics for thin flat-plate wings of aspect ratio greater than one do not appear to be affected by the endplates. The effect of the endplates on the drag characteristics of cambered-plate wings is still under investigation. It is known, however, that endplates do have an effect on the drag and lift characteristics of a cambered Eppler 61 airfoil/wing.

Nomenclature

Symbols

AR	full-span aspect ratio
C_D	drag coefficient (3D)
C_d	section drag coefficient (2D)
C_L	lift coefficient (3D)
C_l	section lift coefficient (2D)
C_{L_α} or C_{l_α}	lift-curve slope
$C_L^{3/2}/C_D$	endurance parameter
$C_{m/4}$	pitching moment coefficient about the quarter chord
C_{m_α}	slope of pitching moment curve
L/D	lift-to-drag ratio
M	resolution of A/D converter
Re_c or Re	root-chord Reynolds number
U_∞	freestream velocity
a	lift-curve slope
a_0	2D lift-curve slope
b	wing span
c	root-chord length
e_Q	quantization error
sAR	semi-span aspect ratio
t	wing thickness
α	angle of attack
$\alpha_{C_L=0}$	zero-lift angle of attack
α_{stall}	stall angle of attack
τ	Glauert parameter

Subscripts

max	maximum
min	minimum

Abbreviations

2D	two-dimensional (airfoil)
3D	three-dimensional (wing)
A/D	analog-to-digital
TE	trailing edge
UND-FB1	old Notre Dame aerodynamic force balance
UND-FB2	new Notre Dame aerodynamic force balance

Paper presented at the RTO AVT Course on "Development and Operation of UAVs for Military and Civil Applications", held in Rhode-Saint-Genèse, Belgium, 13-17 September 1999, and published in RTO EN-9.

Introduction

There is a serious effort to design aircraft that are as small as possible for special, limited-duration military and civil missions. These aircraft, called micro-air vehicles (MAVs) (Davis et al, 1996; Ashley, 1998; Wilson 1998; Dornheim, 1998; Mraz, 1998; and Fulghum, 1998), are of interest because electronic surveillance and detection sensor equipment can now be miniaturized so that the entire payload mass is about 18 grams. The advantages of a MAV include compact system transportable by a single operator, rapid deployment, real-time data, low radar cross-section, difficult to see and very quiet. The potential for low production cost is also an advantage. The primary missions of interest for fixed wing MAVs include surveillance, detection, communications, and the placement of unattended sensors. Surveillance missions include video (day and night) and infrared images of battlefields (referred to as the "over the hill" problem) and urban areas (referred to as "around the corner"). These real-time images can give the number and location of opposing forces. This type of information can also be useful in hostage rescue and counter-drug operations. Because of the availability of very small sensors, detection missions include the sensing of biological agents, chemical compounds and nuclear materials (i.e., radioactivity). MAVs may also be used to improve communications in urban or other environments where full-time line of sight operations are important. The placement of acoustic sensors on the outside of a building during a hostage rescue or counter-drug operation is another possible mission.

The requirements for fixed wing MAVs cover a wide range of possible operational environments including urban, jungle, desert, maritime, mountains and arctic environments. Furthermore, MAVs must be able to perform their missions in all weather conditions (i.e., precipitation, wind shear, and gusts). Because these vehicles fly at relatively low altitudes (i.e., less than 100 m) where buildings, trees, hills, etc. may be present, a collision avoidance system is also required.

The long term goal of this project is to develop aircraft systems with a mass of less than 30 grams, have about an eight centimeter wing span that can fly for 20 to 30 minutes at between 30 and 65 km/hr. The current goal is to develop aircraft with a 15 centimeter wing span that have a mass of about 90 grams. The gross mass of micro-air vehicles and other flying objects versus Reynolds number is shown in Figure 1, with the data from Jackson (1996-97), Taylor (1969-70), and Tennekes (1996). Since it is not possible to meet all of the design requirements for a micro-air vehicle with current technology, research is proceeding on all of the system components at various government laboratories, companies and universities.

Design aims

The design requirements cover a wide range when one considers the diversity of possible applications for micro-air vehicles. The MAV must be designed as a system consisting of airframe, propulsion, payload and avionics. Although much smaller than currently operational UAVs, electrically powered MAVs will have approximately the same weight fractions, that is, 21% for the airframe, 11% for the engine, 30% for the battery, 21% for the payload, and 17% for avionics and miscellaneous items. Minimum wing area for ease of packaging and pre-launch handling is also important. Figure 2 presents the payload mass versus wingspan for MAVs and other larger UAVs.

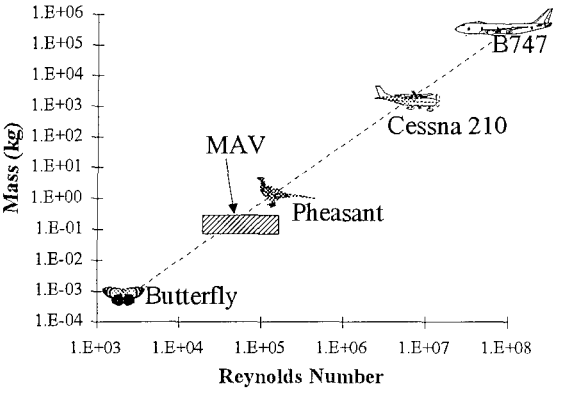

Figure 1: Reynolds number range for flight vehicles

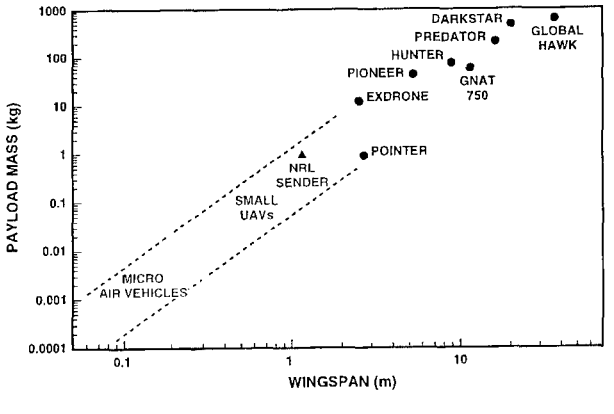

Figure 2: UAV payload vs wingspan (Davis, 1999) (Reprinted with permission of MIT Lincoln Laboratory, Lexington, Massachusetts)

A typical fixed wing MAV mission (Morris, 1997) could include the following sequence of events:

1. Launch and climb to 100 meters
2. High speed dash (64 km/hr Indicated Air Speed) to target (at 40 km/hr head wind)

3. Loiter over target area
4. Maneuver over target during loiter while turning at the minimum radius
5. Descend and climb over target area
6. Climb to 100 meters
7. High speed dash ($64\,km/hr$ Indicated Air Speed) to launch point (tail wind $40\,km/hr$).

Mission constraints in this simulation include duration, operational radius, minimum turning radius, minimum climb angle, maximum altitude and number of climbs. Several MAV designs have been built and flown with this type of mission in mind. A $15\,cm$, square planform internal combustion engine powered vehicle called the Flyswatter has been flown by Morris (1997). A rudder and elevator surfaces are used to control this MAV. The first electric powered $15\,cm$ MAV with proportional radio control carrying a video camera was designed and flown by Matthew T. Keennon of *AeroVironment*. This vehicle called the Black Widow currently holds the record for endurance at 22 minutes (Keennon, 1999). Other MAVs with larger dimensions have been designed and flown to help develop the electronic packages and control systems (Harris, 1999; and Ailinger, 1999). Although these are examples of current vehicles, further improvements will be made when more data on low Reynolds number aerodynamics is available and smaller, more efficient electric motors and propellers have been developed.

The airfoil section and wing planform of the lifting surface occupy a central position in all design procedures for flying vehicles. Therefore, all low Reynolds number vehicles share the ultimate goal of a stable and controllable vehicle with maximum aerodynamic efficiency. Aerodynamic efficiency is defined in terms of the lift-to-drag ratio. Airfoil section $C_{l_{\max}}$, $C_{d_{\min}}$ and $(C_l/C_d)_{\max}$ as a function of Reynolds number are shown in Figures 3a, 3b, and 3c after McMasters and Henderson (1980). It is clear from this figure that airfoil performance deteriorates rapidly as the chord Reynolds number decreases below $100,000$. While the maximum lift-to-drag ratio for most low-speed fixed-wing aircraft ($U_\infty < 50\ m/s$) is greater than 10, values for insects and small birds are usually less than 10. Furthermore, to achieve these values for MAVs at low Reynolds numbers, the wings must emulate bird and insect wings and be very thin (i.e., $t/c < 0.06$) with a modest amount of camber.

Requirements for a typical propeller driven MAV, for example, include long flight duration (i.e., high value of $C_L^{3/2}/C_D$ at speeds up to $65\,km/hr$ at chord Reynolds numbers from about $45,000$ to $180,000$ and altitudes from 30 to 100 meters). Since these vehicles are essentially small flying wings, there is a need to develop efficient low Reynolds number, low aspect-ratio wings which are not overly sensitive to wind shear, gusts, and the roughness produced by precipitation. Furthermore,

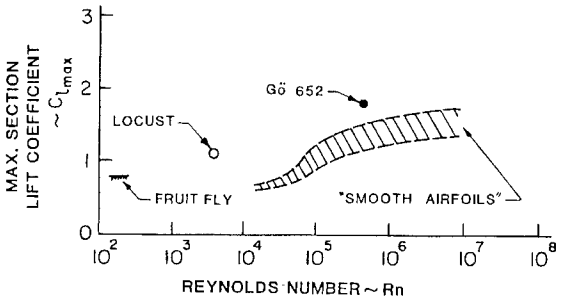

(a) Maximum lift coefficient

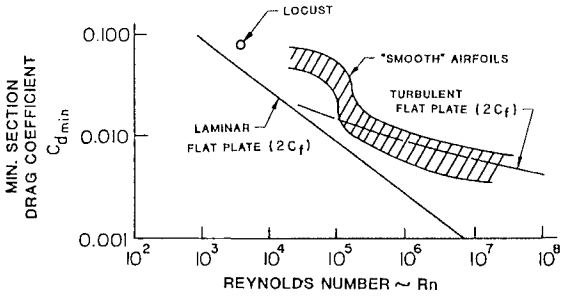

(b) Minimum drag coefficient

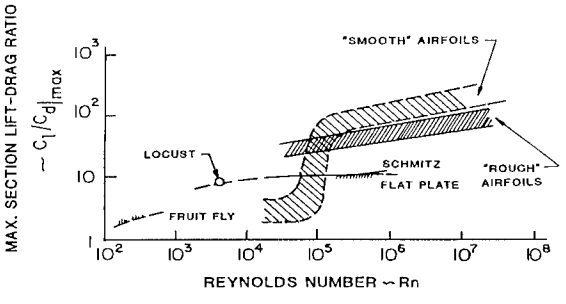

(c) Maximum lift-to-drag ratio

Figure 3: Airfoil performance (McMasters and Henderson, 1980)

confidence that the operational vehicle will perform as designed is important in all applications.

Flow problems

Although design methods developed over the past 35 years produce efficient airfoils for chord Reynolds numbers greater than about 200,000, these methods are generally inadequate for chord Reynolds numbers below 200,000, especially for very thin airfoils. In relation to the airfoil boundary layer, important areas of concern are the separated regions which occur near the leading and/or trailing edges and transition from laminar to turbulent flow if it occurs. It is well known that separation and transition are highly sensitive to Reynolds number, pressure gradient, and the disturbance environment. Transition and separation play a critical role in determining the development of the boundary layer which, in turn, affects the overall performance of the airfoil. The aerodynamic characteristics of the wing and other components in turn affect the static, dynamic and aeroelastic stability of the entire vehicle. Therefore the successful management of the sensitive boundary layer for a particular low Reynolds number vehicle design is critical.

The survey of low Reynolds number airfoils by Carmichael (1981), although almost two decades old, is a very useful starting point in the description of the character of the flow over airfoils over the range of Reynolds numbers of interest here. The following discussion of flow regimes from $1,000 \leq Re_c \leq 200,000$ is a modified version of Carmichael's original work.

- In the range between $1,000 \leq Re_c \leq 10,000$, the boundary layer flow is laminar and it is very difficult to cause transition to turbulent flow. The dragon fly and the house fly are among the insects that fly in this regime. The dragon fly wing has a sawtooth single surface airfoil. It has been speculated that eddies in the troughs help keep the flow from separating. The house fly wing has large numbers of fine hair-like elements projecting normal to the surface. It is speculated that these promote eddy-induced energy transfer to prevent separation. Indoor rubber-powered type model airplanes also fly in this regime. It has been found that both blunt leading and trailing edges enhance the aerodynamic performance.

- For chord Reynolds numbers between 10,000 and 30,000, the boundary layer is completely laminar and artificial tripping has not been successful. Experience with hand-launched glider models indicates that when the boundary layer separates it does not reattach.

- The range $30,000 \leq Re_c \leq 70,000$ is of great interest to MAV designers as well as model aircraft builders. The choice of an airfoil section is very important in this regime since relatively thick airfoils (i.e., 6% and above) can have significant hysteresis effects caused by laminar separation with transition to turbulent flow. Also below chord Reynolds numbers of about 50,000, the free shear layer after laminar separation normally does not transition to turbulent flow in time to reattach. Near the upper end of this range, the critical Reynolds number can be decreased by using boundary layer trips. Thin airfoil sections (i.e., less than 6% thick) at the upper end of this regime can exhibit reasonable performance.

- At Reynolds numbers above 70,000 and below 200,000, extensive laminar flow can be obtained and therefore airfoil performance improves although the laminar separation bubble may still present a problem for a particular airfoil. Small radio controlled model airplanes fly in this range.

- Above Re_c of 200,000, airfoil performance improves significantly and there is a great deal of experience available from large soaring birds, large radio controlled model airplanes, human powered airplanes, etc.

Laminar separation bubbles occur on the upper surface of most airfoils at Reynolds numbers above about 50,000. These bubbles become larger as the Reynolds number decreases, usually resulting in a rapid deterioration in performance, i.e., substantial decrease in L/D. In principle the laminar separation bubble and transition can be artificially controlled by adding the proper type of disturbance at the proper location on the airfoil. Wires, tape strips, grooves, steps, grit, or bleed-through holes in the airfoil surface have all been used to have a positive influence on the boundary layer in this critical Reynolds number region. The type and location of these so-called "turbulators" and their actual effect on the airfoil boundary layer has not been well documented. Furthermore, the addition of a turbulator *does not always* improve the airfoil performance. In fact, how the disturbances produced by a given type of turbulator influence transition is not completely understood.

As a result of this critical boundary layer behavior, several important questions must be addressed:

1. What is the free stream disturbance level and flight environment for a given low Reynolds number application?

2. If the flight conditions are known and a suitable design technique was available, could the resulting vehicle or component be adequately evaluated in a wind tunnel which, in general, has a different disturbance level and environment than the flight condition?

3. Is the hysteresis in aerodynamic forces observed in low turbulence wind tunnel experiments present in powered applications (i.e., do structural vibrations originating with the propulsion or drive system affect boundary layer transition)?

4. Because the critical quantities measured in wind tunnel experiments are very small, what is the level of accuracy needed to improve design and analysis methods?

Preliminary experiments

Many of the problems plaguing very low Reynolds number research involve the difficulties associated with making accurate wind/water tunnel models and obtaining reliable data. Because the boundary layers are sensitive to small disturbances, accurate wind/water tunnel models are very important in the evaluation of a given design. Furthermore, because the forces, pressure differences and velocities are extremely small, a great deal of care must be exercised to obtain accurate and meaningful data. Low Reynolds number aerodynamic research has been in progress at the University of Notre Dame since 1978. However, chord Reynolds numbers below about 80,000 were seldom of interest in the studies before 1996. Also, most of the studies were for relatively thick airfoils, e.g. the 11% thick Lissaman 7769, the 13% thick Miley M06-13-128, and the 13% thick Wortmann FX 63-137 airfoils. The only relatively thin airfoils studied were the Eppler 61 and Pfenninger 048 airfoils. The Eppler 61, shown in Figure 4, was originally designed for model airplanes with a chord Reynolds numbers of about 80,000 and has a thickness of 5.63% and 6.3% camber. Figure 5 shows a schematic of the Pfenninger 048 airfoil geometry tested by Burns (see Burns, 1981). This airfoil has a thickness-to-chord ratio of 4.8% and a 4.2% camber.

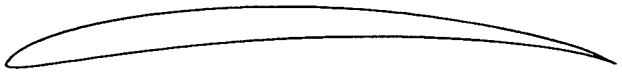

Figure 4: Eppler 61 airfoil profile

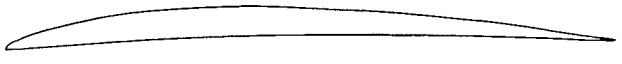

Figure 5: Pfenninger 048 airfoil profile

The wind tunnel data shown in Figure 6 for the Eppler 61 and the Pfenninger 048 airfoils was obtained in 1980 and published by Burns (1981) and Mueller and Burns (1982). Figure 6 indicates that for chord Reynolds numbers below 90,000, the thinner and sharper leading edge Pfenninger airfoil performs better than the Eppler 61 airfoil.

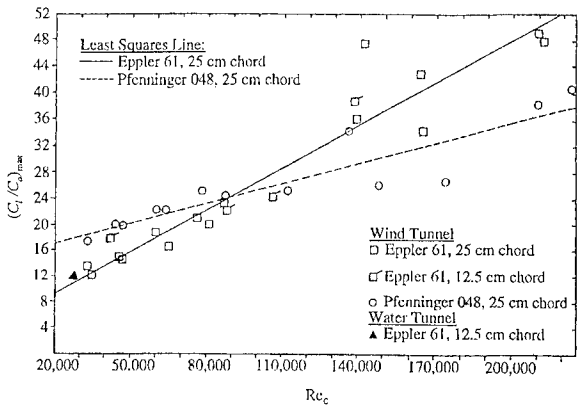

Figure 6: Maximum lift-to-drag ratio versus chord Reynolds number for the two-dimensional Eppler 61 and Pfenninger 048 airfoils (Burns, 1981)

Burns also studied the flowfield over the Eppler 61 airfoil for different Reynolds numbers using the smoke wire technique. The location of the boundary layer separation could be obtained from his flow visualization photographs. Figure 7 shows the effect of changing the angle of attack on the boundary layer for $Re_c = 46,000$.

Flow visualization was also conducted on the Pfenninger 048 airfoil at different Reynolds numbers and different angles of attack. Figure 8 shows examples of the flow visualization images for $Re_c = 47,000$.

A new series of experiments was performed in the Spring of 1997 to evaluate several thin airfoil shapes using the existing strain gauge force balance (UND-FB1) in the Hessert Center water tunnel. The results for lift and drag from these experiments down to a chord Reynolds of 25,000 were very encouraging. A more complete experimental study of one of these airfoil shapes (i.e., the Eppler 61) was performed during the summer of 1997 (Prazak and Mueller, 1997). These experiments covered the Reynolds number range from 12,000 to 63,000. Hydrogen bubble flow visualization was used to determine the location of boundary layer separation and the existing wind tunnel lift/drag force balance (UND-FB1) was used to make aerodynamic measurements. All of these 2D experiments included two endplates. The $(C_l/C_d)_{\max}$ for the 2D Eppler 61 from these water tunnel experiments is included in Figure 6 (▲). The results of the Prazak and Mueller study in the water tunnel indicated that by adding a computer data acquisition system to the UND-FB1 force balance, the uncertainty in the force measurements down to $Re_c = 20,000$ could be reduced significantly for the full span models.

Scope of present study

The purpose of the present work is to present and discuss the measurement problems associated with small aspect ratio wings at Reynolds numbers below 200,000.

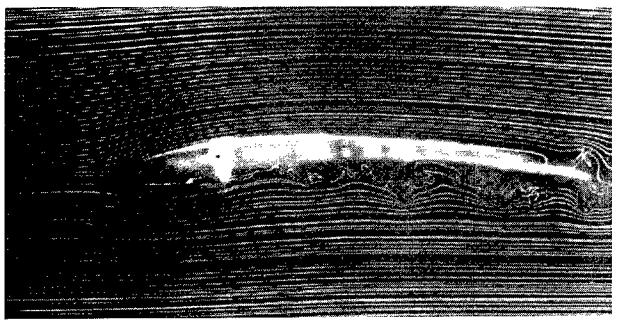

(a) $\alpha = 0^\circ$

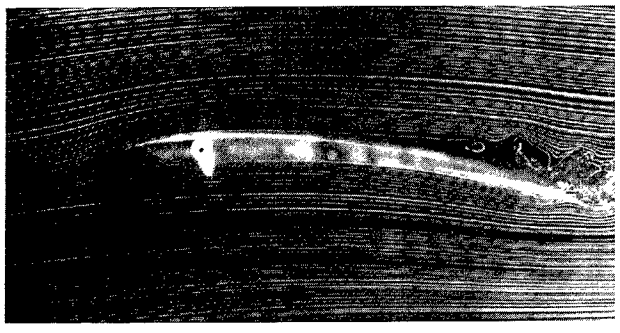

(b) $\alpha = 4^\circ$

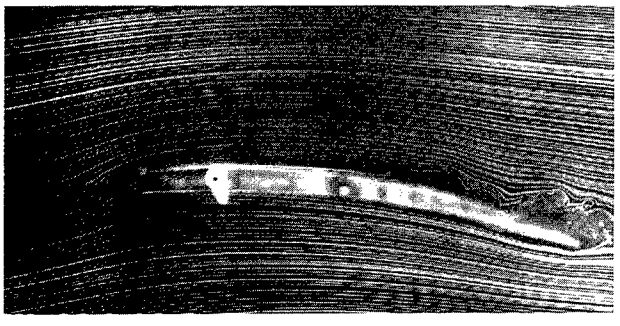

(c) $\alpha = 8^\circ$

Figure 7: Smoke flow visualization on Eppler 61 airfoil at $Re_c = 46,000$ (Burns, 1981)

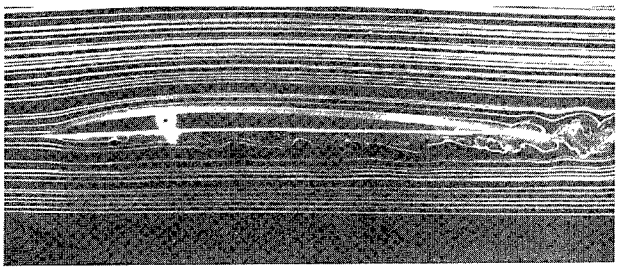

(a) $\alpha = 0^\circ$

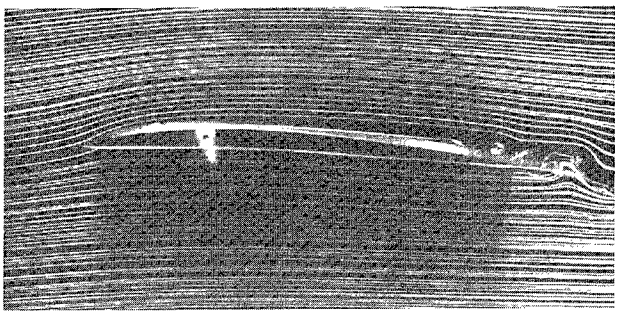

(b) $\alpha = 4^\circ$

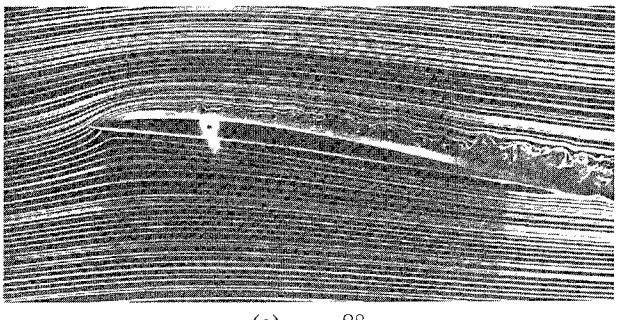

(c) $\alpha = 8^\circ$

Figure 8: Smoke flow visualization on Pfenninger 048 airfoil at $Re_c = 47,000$ (Burns, 1981)

Both wind tunnel and water tunnel experiments were performed in an attempt to acquire 2D airfoil and finite low aspect ratio wing data. Studies of the effect of two endplates on the results for 2D configurations and one endplate for semi-span or half models were also made.

Apparatus and procedures

Wind tunnel

The Hessert Center for Aerospace Research is equipped with two similar, horizontal, subsonic open-circuit wind tunnels. Each indraft tunnel has a contraction ratio of 20.6:1. The cross-sections of the entrance and test section are square. The largest test section is two feet by two feet (61 cm by 61 cm). The contraction cones are designed to provide very low turbulence levels in the test section. Just ahead of the contraction cone are twelve anti-turbulence screens. Both the contraction cone and the test sections are mounted on rollers to provide an easy means of interchanging these components. Downstream of the test section is the diffuser which is fixed into the wall of the laboratory. The diffuser decelerates the air and also gradually transforms the square contour to a circle. The impeller is driven by a variable speed electric motor. By varying the speed of the motor, the tunnel speed may reach a maximum of approximately $120\,ft/sec$ $(36.6 m/s)$ with a four square foot test section $(3,221\,cm^2)$. The test sections used are six feet (1.82 meters) in length. All wind tunnel experiments presented in this report were conducted in one of these subsonic wind tunnels. The range of velocities required for tests up to $Re_c = 200,000$ could easily be obtained. In general, the minimum velocity for force balance measurements was kept above $5\,m/s$ $(16.4\,ft/s)$. Figure 9 is a schematic of the wind tunnel used. The freestream turbulence intensity was approximately 0.05% over the range of interest.

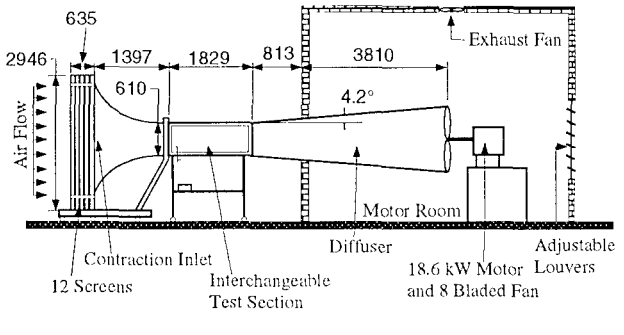

Figure 9: Schematic of the low-speed wind tunnel (all dimensions in mm)

Water tunnel

For tests between $20,000 \leq Re_c \leq 80,000$, an Eidetics® free-surface water tunnel with a $15\,in \times 18\,in$ $(38.1\,cm \times 45.7\,cm)$ test section, pictured in Figure 10, was used. The water tunnel is also located in the main laboratory of the Hessert Center. Water velocities up to $1.28\ ft/sec$ $(39\ cm/sec\ )$ can be obtained in the test section. A freestream turbulence intensity of less than 1% has been reported by the manufacturer of the water tunnel.

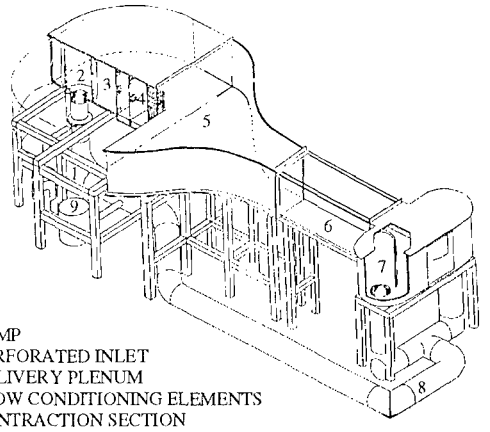

Figure 10: Schematic of the flow visualization water tunnel (Eidetics®)

Flow visualization techniques

A qualitative visual examination of the flow as it passes an airfoil is key in understanding its quantitative aerodynamic characteristics. In the wind tunnel, two different methods can be used to generate smoke for this flow visualization. With the first method, smoke is generated by a device which allows kerosene to drip onto electrically heated filaments; the smoke is then funneled to a smoke rake. The rake has a filter bag and cooling coils which reduce the smoke temperature to approximately ambient before passing through the anti-turbulence screens and into the test section. With the second method, a fine wire is placed upstream of the model. This wire is coated with oil and an electric current is applied to the wire. As the wire gets heated, the small beads of oil formed on the wire burn, which gives rise to fine smoke streaklines. This technique, which has been described in more details by Batill and Mueller (1980), is referred to as the *smoke-wire* technique. The water tunnel is excellent for flow visualization using either the hydrogen bubble or dye injection technique. A Kodak DC120 digital camera and CCD video cameras are available to capture flow visualization results.

Description of the UND-FB1 balance

Most of the results on thin plates were obtained with the existing three-component platform aerodynamic balance UND-FB1. This balance can be used to measure lift, drag and pitching moment about the vertical axis. The balance is an external balance placed on top of the test section of either of the two low-speed wind tunnels. With this balance, lift and drag forces are transmitted through the sting which is mounted directly to the moment sensor. The moment sensor is rigidly mounted to the adjustable angle of attack mechanism on the top platform. The lift platform is supported from the drag platform by two vertical plates that flex only in the lift direction. The lift and drag platforms are also connected with a flexure with bonded foil strain gauges mounted on it. The drag platform is supported by two vertical plates that flex only in the drag direction and hang from two more vertical flexible plates attached to the base platform of the balance. The base and drag platforms are also connected by a flexure with strain gauges mounted on it. For this balance a second set of flexures, for both lift and drag, are engaged when the loads are large. For the range of forces measured in this investigation, the second set of flexures was never engaged. Figure 11 shows a schematic of the old balance setup in the wind tunnel. The arrangement with two endplates shown in Figure 11 is known as arrangement number 1. Arrangement number 2, not shown, has the lower endplate removed for the semi-infinite tests.

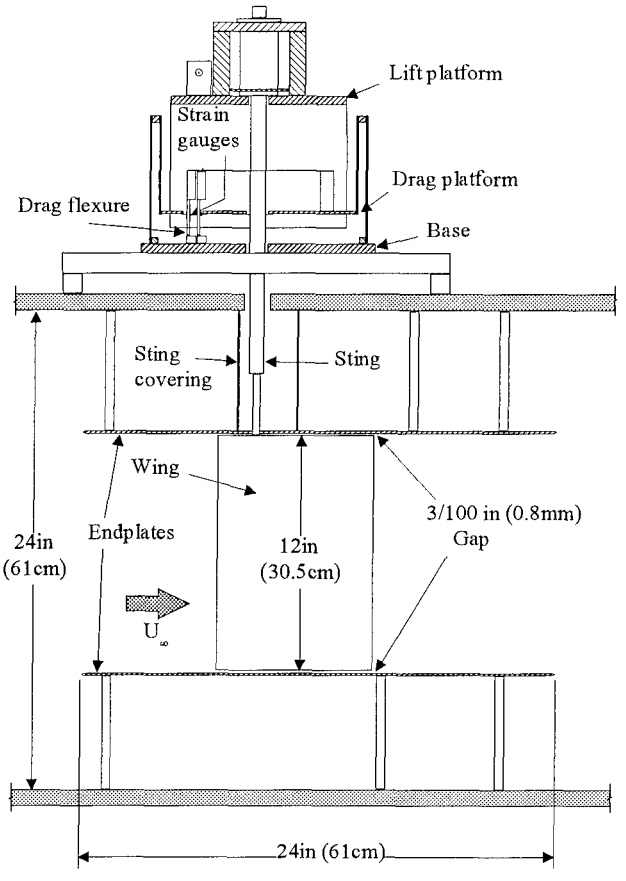

Figure 11: UND-FB1 balance arrangement (1) with two endplates in the wind tunnel

Thin-plate models for current investigation

Keeping in mind the objective of this first phase of the investigation which was to study the aerodynamic characteristics of small, low aspect-ratio flat and cambered wings, several thin, flat and cambered rectangular aluminum models with a thickness-to-chord ratio of 1.93% were built. Thin models were selected because birds and insects have very thin wings. The models either had a 5-to-1 elliptical leading edge and a 3° tapered trailing edge, or 5-to-1 elliptical leading and trailing edges. The cambered models had a circular arc shape with 4% camber. The semi-span aspect ratios (sAR) tested varied between 0.50 and 3.00. The root-chord length of the models was either $4\,in$ $(10.2\,cm)$ or $8\,in$ $(20.3\,cm)$. Figure 12 shows schematics of the airfoil geometries for the wings with a tapered trailing edge, while Table 1 gives the dimensions of the different models used. With the nomenclature used for the wing designation, the first four characters define the nominal dimensions of the model. For instance, C8S4 means a **C**hord of $8\,in$ and a **S**pan of $4\,in$. The following characters, if any, define the shape: a **C** means a cambered plate and **E** means an elliptical trailing edge instead of a tapered trailing edge. A maximum span of $12\,in$ $(30.5\,cm)$ was chosen so that these models could be used in both the wind and water tunnels.

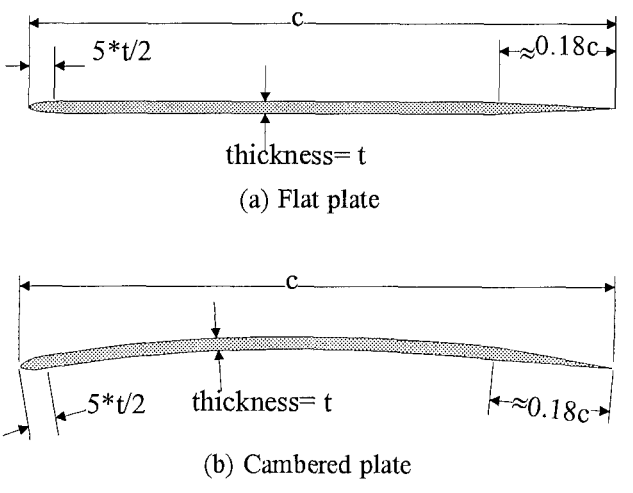

Figure 12: Airfoil geometry for models with tapered trailing edge

Designation	Chord (in)	Span (in)	sAR	Thickness (in)	Camber (%)
C8S4	7.973	3.998	0.5	0.155	0
C8S8	7.973	8.003	1.0	0.154	0
C8S12	7.985	12.01	1.5	0.157	0
C4S8	3.999	8.019	2.0	0.077	0
C4S12	4	12.014	3.0	0.077	0
C8S4C	7.975	3.995	0.5	0.156	4
C8S8C	7.983	8	1.0	0.156	4
C8S12C	7.908	12.013	1.5	0.156	4
C4S8C	3.995	8	2.0	0.078	4
C4S12C	3.936	11.998	3.0	0.079	4
C8S12E	7.969	12.011	1.5	0.156	0
C8S12CE	7.931	12.011	1.5	0.157	4

C: cambered; E: elliptical trailing edge

Table 1: Wing dimensions

Tunnel configurations

Endplates were mounted in the wind and water tunnels. The plates could be removed to simulate either a semi-infinite model or a finite model. All wings tested were held at the quarter-chord point and the sting was covered by a streamlined sting covering in the wind tunnel and a cylindrical covering in the water tunnel. The gaps between the wing and the endplates were adjusted to approximately $0.03in$ ($0.8mm$). Mueller and Burns (1982) showed that gap sizes varying between 0.1 mm and 1.4 mm are usually acceptable and do not affect the results. Furthermore, Rae and Pope (1984) suggest that the gap be less than $0.005 \times$ span. For a $12in$ ($30.5cm$) span model, this corresponds to a maximum gap size of $0.06in$ (1.5 mm), which is larger than the gap used in the current investigation. All 2D tests (or infinite wing/airfoil tests) were performed with both endplates present. For semi-infinite wings (denoted by the semi-span aspect ratio symbol sAR), the bottom plate was removed. Finally, for finite wing tests (denoted by the aspect ratio symbol AR), both endplates and the sting covering were removed.

Data acquisition system with UND-FB1 balance

Signals from the strain gauges were measured with very sensitive instrumentation. The strain gauges were configured in a full Wheatstone bridge. An excitation voltage of 5 V was used for all the strain gauge bridges. The bridge signals were read with an instrumentation amplifier circuit, with available gains from 1 to 8,000. The amplified analog signals were sent to the computer where they were then converted using a four-channel, 12-bit A/D converter from *United Electronic Industries* (UEI). Four data channels (lift, drag, moment and dynamic pressure) could be measured. All the data was acquired using a PC-based data acquisition system running the LABVIEW® 5 graphical programming language. The angle of attack was controlled manually with the UND-FB1 balance.

Procedure for data acquisition

Before measuring any aerodynamic force and moment with either balance, the amplifier gains were adjusted to maximize the output signals that were expected during a given set of experiments. The balance was then calibrated using known masses. The lift, drag and moment axes were all independent.

For tests looking at the aerodynamic characteristics as a function of angle of attack, the tunnel velocity was adjusted with the model at $\alpha = 0°$ to yield the desired nominal Reynolds number. The angle of attack was then, in general, set to $\alpha = -15°$. Data was taken for angles of attack up to a large positive angle by an increment of $1°$. The wing was then brought back to $\alpha = 0°$ by an increment of $-1°$ in order to see if hysteresis was present. Offset readings were measured for all four data acquisition channels before the tunnel was turned on with the model at $\alpha = 0°$. At the end of the run, the tunnel was turned off with the model at $\alpha = 0°$ and drift readings were obtained for all channels. The offset voltage for a given channel was subtracted from all the voltage readings for that channel. A percentage of the drift was also subtracted from all the readings. A linear behavior was assumed for the drift. This means that if n angles of attack were tested with the tunnel running, $1/n \times$ drift was subtracted from the first point, $2/n \times$ drift was subtracted from the second point, and so forth. Other procedures related to specific applications will be presented in the text when appropriate.

Measurement uncertainty with balance UND-FB1

Uncertainties in the measurements were computed using the Kline-McClintock technique (Kline and McClintock, 1953) for error propagation. The two main sources of uncertainty were the quantization error and the uncertainty arising from the standard deviation of

a given mean output voltage. The quantization error is $e_Q = \frac{1}{2}\left[\frac{\text{Range in volts}}{2^M}\right]$, where M is the number of bits of the A/D converter. Optimizing the range of the output voltages can help to reduce the uncertainties. If the gain is increased, the standard deviation of the mean will also be increased, but the ratio of the standard deviation to the mean will basically remain the same. However, the uncertainty from the quantization error will be reduced because the quantization error is a fixed value (a function of the range and the resolution of the A/D converter). The ratio of the quantization error to the mean voltage will then be smaller if a larger gain is used and a larger balance output mean voltage is obtained.

The uncertainty in the angle of attack was determined to be on the order of $0.2° - 0.3°$. Figures 13 through 15 show an example of uncertainties obtained at $Re_c = 60,000$ with the cambered plates. Error bars indicate the uncertainty in C_L, C_D and $C_{m/4}$. The average uncertainties from $\alpha = 3°$ and up are approximately 6% to 7% for C_L and C_D and 10% for $C_{m/4}$.

New force/moment aerodynamic balance UND-FB2

Description

A new platform force/moment balance was designed by Matt Fasano, Professional Specialist at the Hessert Center for Aerospace Research, and built for the aerodynamic studies on low aspect-ratio wings down to chord Reynolds numbers of 20,000. The design of this new balance (UND-FB2) was based on the existing balance (UND-FB1) and measures lift, drag, and pitching moment about the vertical axis. It is an external balance placed on top of the test section for either of the two low-speed wind tunnels or the water tunnel. Due to the better sensitivity of the newly designed balance (UND-FB2), only this balance is now used with the water tunnel.

With this balance, lift and drag forces are transmitted through the sting which is mounted directly to the moment sensor (see Figure 16 for a schematic of the new balance). The moment sensor is rigidly mounted to the adjustable angle of attack mechanism on the top platform. The lift platform is supported from a platform, called the drag platform, by two vertical plates that flex only in the lift direction. The lift and drag platforms are also connected with a $1/8\,in \times 3/8\,in \times 1.5\,in$ $(3.2\,mm \times 9.5\,mm \times 38.1\,mm)$ flexure with bonded foil strain gauges mounted on it. The drag platform is supported by two vertical plates that flex only in the drag direction and hang from two more vertical flexible plates attached to the base platform of the balance. The base and drag platforms are also connected by a $1/16in \times 3/8in \times 1.5in\,(1.6mm \times 9.5mm \times 38.1mm)$ flexure with strain gauges mounted on this drag flexure. Both flexures act like cantilever beams when loads are applied to the balance.

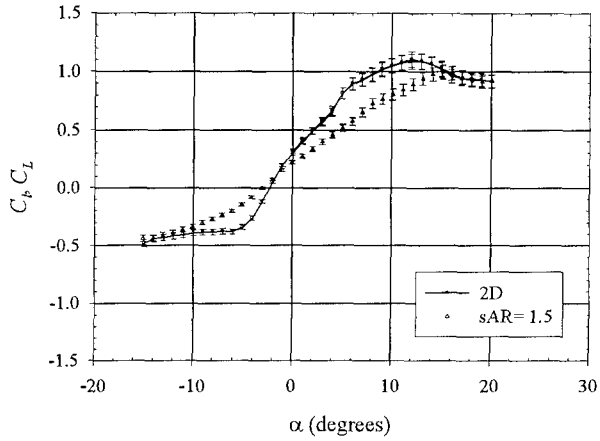

Figure 13: Uncertainties in lift coefficient for cambered plates at $Re_c = 60,000$ with UND-FB1

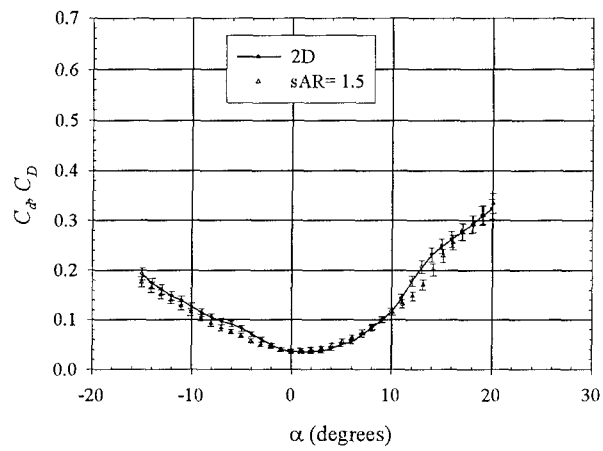

Figure 14: Uncertainties in drag coefficient for cambered plates at $Re_c = 60,000$ with UND-FB1

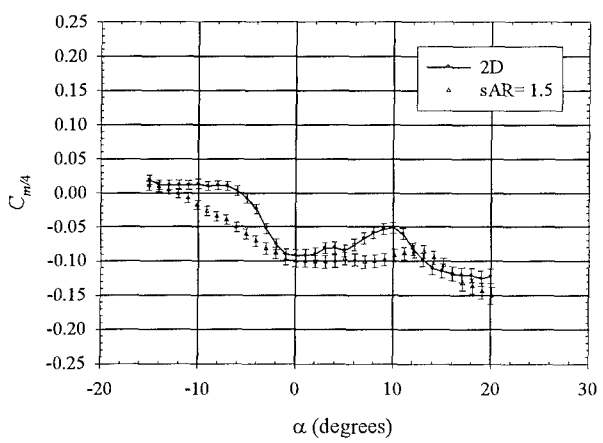

Figure 15: Uncertainties in pitching moment coefficient for cambered plates at $Re_c = 60,000$ with UND-FB1

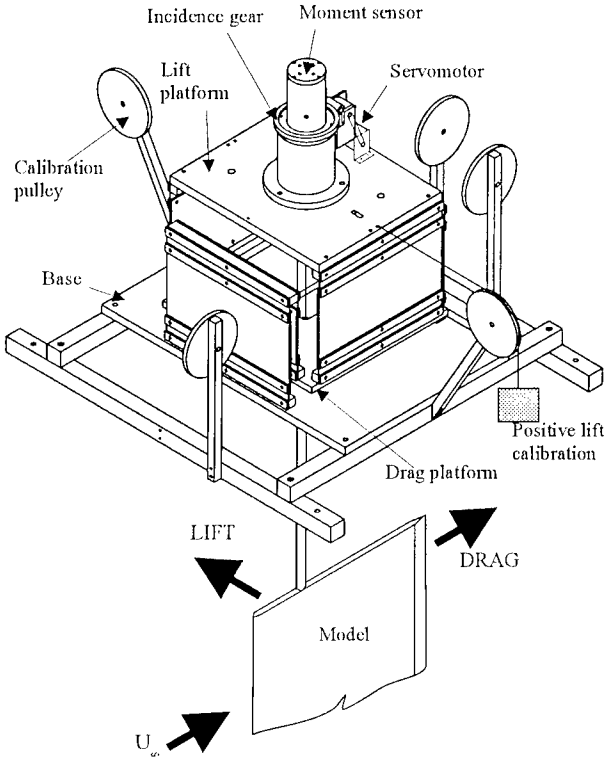

Figure 16: Schematic of the new balance UND-FB2

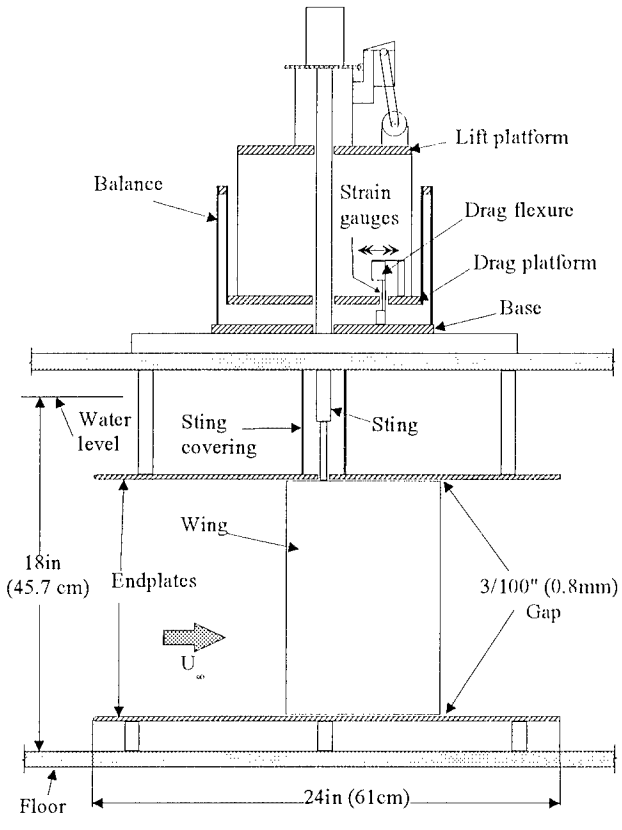

Figure 17: New-balance arrangement (1) in the water tunnel with two endplates

As mentioned earlier, endplates were mounted in both wind and water tunnels. Figure 17 shows a schematic of the new balance with the endplates in place in the water tunnel. All wings tested were held at the quarter-chord point and the sting was covered by a streamlined sting covering in the wind tunnel and a cylindrical covering in the water tunnel.

The moment sensor is a *Transducer Techniques* RTS-25 reaction torque sensor. This torque sensor uses bonded foil strain gauges and is rated at $1.5mV/V$ output. The maximum rated capacity is $25\,oz \cdot cm$ $(17.7\,N \cdot cm)$ and a torsional stiffness of $1,324\,N \cdot cm/\text{rad}$. The moment sensor is attached to an adjustable angle of attack mechanism powered by a servomotor with a controller.

Electronics

Signals from the strain gauges are measured with very sensitive instrumentation. The strain gauges for the drag and lift flexures are 350 ohms with a G-factor of 2.09 and are configured in a full Wheatstone bridge. An excitation voltage of $5\,V$ is used for all the strain gauge bridges. The bridge signals are read with an instrumentation amplifier circuit with a gain as high as 8,000. Due to the sensitivity of the circuit many precautions were made to reduce noise. At first, Ni-Cd rechargeable batteries were used to power the amplifiers, analog-to-digital converters, and the excitation voltage for the strain gauges. A DC power supply is now being used because of the quick discharge of the batteries during data acquisition. The batteries used could not provide a constant voltage for several hours.

The amplifiers and analog-to-digital converters are mounted on a circuit board placed in a control box with switches and potentiometers (pots) to adjust the gains, offsets and balance the Wheatstone bridges. Four data channels (lift, drag, moment and dynamic pressure when necessary) can be measured quasi-simultaneously. The input differential signal from each channel is sent through two amplifiers from *Analog Devices*: a precision instrumentation AD624 amplifier (gain of 1, 100, 200 or 500) and a software programmable AD526 gain amplifier (gain of 1, 2, 4, 8 or 16). The amplified analog single-ended signals from the four channels are then converted to digital signals using a *Burr-Brown* AD7825, four-channel, 16-bit analog-to-digital converter. The signals are then sent to a *National Instruments* digital data acquisition card (NIDAQ) in a data acquisition computer. The amplified single-ended analog signals can also be sent directly to the computer, thus bypassing the 16-bit A/D converters; the signals are then converted using the four-channel, 12-bit A/D UEI converter, mentioned earlier. With the 16-bit A/D system, each amplifier circuit is identical except for the fourth channel where the amplifiers can be bypassed and a single-ended signal can be sent directly to the 16-bit A/D converter. Figure 18 is a simplified schematic of

the electronic circuitry used.

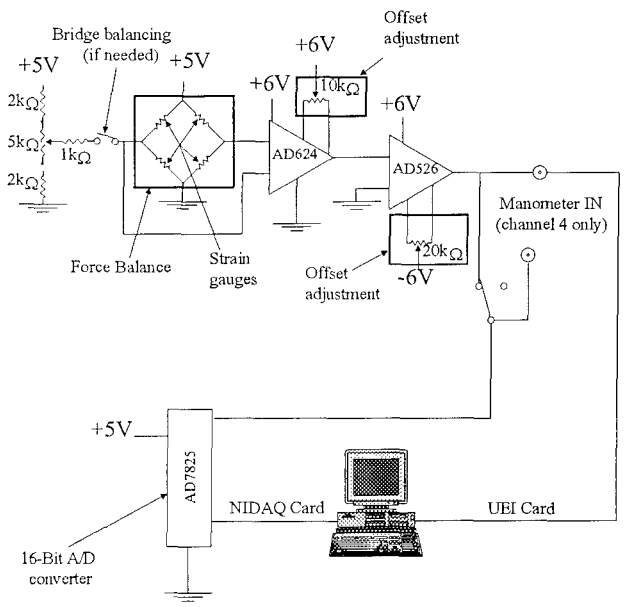

Figure 18: UND-FB2 balance electronics

Data acquisition

All the data was acquired using a PC-based data acquisition system running the LABVIEW® 5 graphical programming language. The NIDAQ card was first used for data acquisition. The UEI card is now used with the new balance when severe noise interferes with the data and the NIDAQ card cannot be used.

The data acquisition process with the new balance was automated. The angle of attack can be automatically varied from a pre-determined list of angles of attack. The range is usually adjusted in order to be able to observe stall.

Specifications

Since the force/moment balance includes very sensitive flexures and strain gauges, the applied forces and moment cannot exceed certain limits. These limiting forces and moment were determined conservatively and are listed in Table 2. The limiting forces and moment for the UND-FB1 balance are also included for comparison (see Huber, 1985). In order to be able to move the balance and mount the models without permanently deforming the flexures, locking pins are used to restrain the balance. These locking pins must be removed when taking data.

Sources of noise

For all measurements, digital filtering in LABVIEW® was necessary to reduce noise generated by the servomotor used to change the angle of attack, and also the motor of the water tunnel when water tunnel tests were performed. A low-pass Butterworth filter with a cut-off frequency of 50 Hz and of order 5 was used. A study on the effect of the filter and its order showed that the mean voltages were basically not affected, but the standard deviations of the means were greatly reduced. It was discovered during preliminary calibrations with the NIDAQ card that the servomotor was causing noise in the data. With the motor ON, the standard deviations of the samples (4,000 data points measured at a sampling frequency of 500 Hz) were larger than those without the motor ON, although the mean values, thus the calibration coefficients, were the same. It was found that isolating the motor from the balance helped to reduce the standard deviations. A thin plastic sheet was then placed between the aluminum motor support and the aluminum top plate, lift platform, of the balance. Moreover, plastic screws were used to mount the motor support to the balance. This eliminated any aluminum/aluminum contact between the motor and the balance. Noise caused by a metal-to-metal contact between a force/moment balance and a motor was also detected in a previous investigation at the University of Notre Dame (Pelletier, 1998). Figure 19 shows the standard deviations of the samples for a lift channel calibration example with and without the isolation plastic.

	UND-FB2	UND-FB1
Positive lift	7.0 N	39.2 N
Negative lift	-3.5 N	-14.7 N
Positive drag	2.0 N	14.7 N
Moment	15.0 $N \cdot cm$	226 $N \cdot cm$

Table 2: Maximum force/moment balance specifications

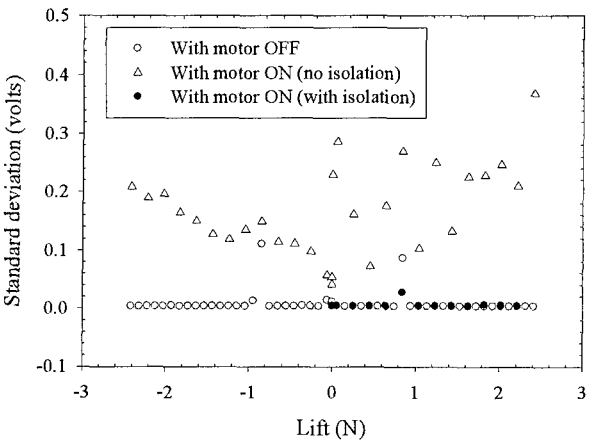

Figure 19: Effect of the motor on the standard deviation with NIDAQ data acquisition card

Calibration

After construction of the balance and electronics, calibrations were performed to ascertain the linearity of the balance for all its *independent* axes: lift, drag and moment. These calibrations were performed by moving the upper plate, lift platform, of the balance or by applying a torque to the moment sensor by placing precision weights of known mass in a container connected to the plate, or moment sensor. The container was connected to the upper plate by running a string over the calibration pulley aligned with the axis to calibrate (for lift and drag) or perpendicular to the torque applicator (pin connected to the sting used to apply a known torque) for the moment calibration. For this moment calibration, the lift and drag locking pins were used to prevent movement in the lift and drag direction as a moment was applied to the sensor. Several calibrations were performed to look for repeatability and linearity. Figures 20 through 22 show examples of the calibration curves that were repeatedly obtained.

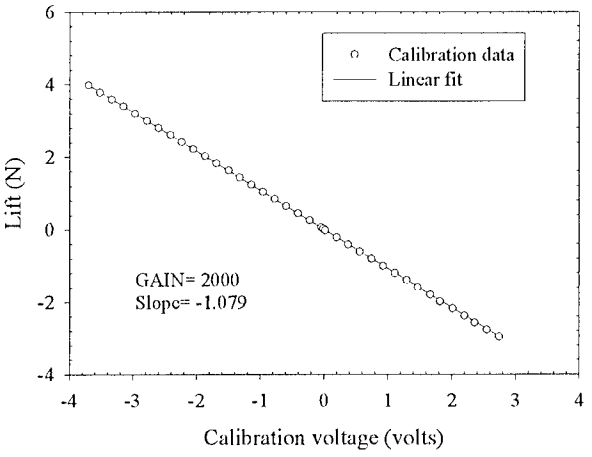

Figure 20: Lift calibration for the new balance

UND-FB2 performance

Once the new balance and its electronics were built and calibrations had been performed, it was tested to see if the results compared to published data. All results presented in this paper have been corrected for solid blockage, wake blockage and streamlined curvature using techniques presented by Pankhurst and Holder (1952) and Rae and Pope (1984). A series of two-dimensional tests were conducted on different models.

Models

In the balance validation phase, two circular cylinders were tested. The diameters of the two cylinders were $0.75\,in$ $(1.9\,cm)$ and $1.255\,in$ $(3.2\,cm)$ and they both had a length of $12\,in$ $(30.5\,cm)$. An Eppler 61 airfoil model, whose profile was shown in Figure 4, was also used to test the balance. The model also had a length of $12\,in$ $(30.5\,cm)$ and a chord of $4.906\,in$ $(12.5\,cm)$.

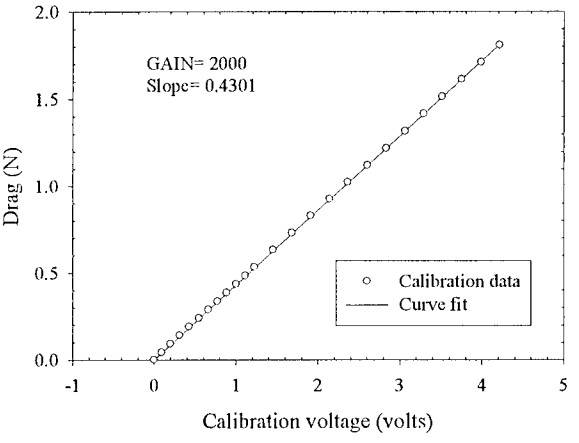

Figure 21: Drag calibration for the new balance

Cylinder results

The new balance was first tested by measuring the two-dimensional drag on two circular cylinders in the low-speed wind tunnel. Figure 23 shows the drag coefficient as a function of Reynolds number. Results of the present investigation were compared to results by Wieselsberger, digitized from *Boundary-Layer Theory* by Schlichting (1979). There is a good agreement between the two sets of data.

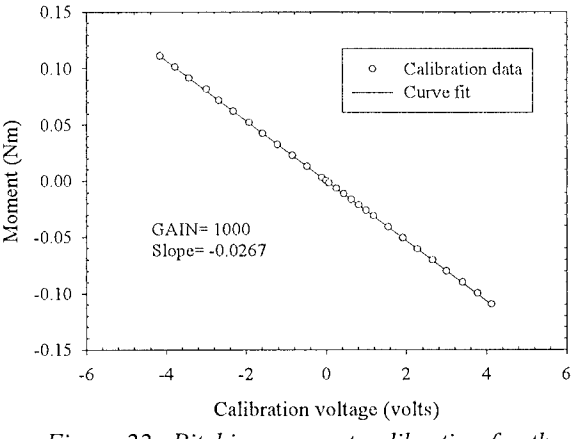

Figure 22: Pitching moment calibration for the new balance

Eppler 61 airfoil results

The balance was then tested by measuring the two-dimensional lift and drag on the Eppler 61 airfoil. Results

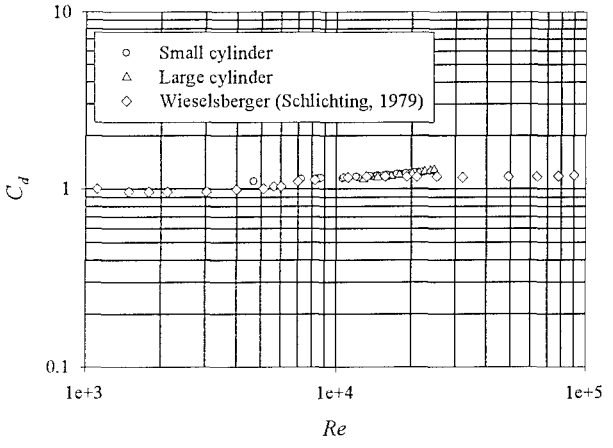

Figure 23: 2D drag coefficient of two circular cylinders with UND-FB2

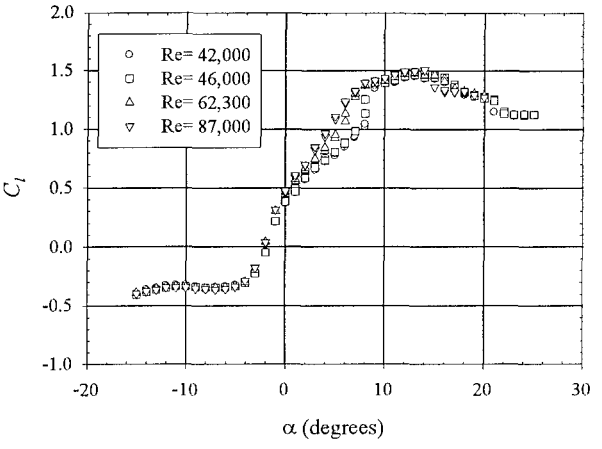

Figure 24: 2D lift coefficient on the Eppler 61 airfoil in the wind tunnel with UND-FB2

were obtained in the wind tunnel and the water tunnel for several Reynolds numbers. Figures 24 and 25 show the two-dimensional lift and drag coefficients respectively in the wind tunnel for different *nominal* Reynolds numbers, i.e., values used to adjust the velocity in the tunnel with the model at $\alpha = 0°$.

Results for C_l indicate a significant difference between results at $Re_c > 60,000$ and those for $Re_c < 60,000$. For large Re_c, C_l increases smoothly with angle of attack α. For smaller Re_c, the lift-curve slope C_{l_α} is smaller for $2° \leq \alpha \leq 8°$ and there is a sharp rise in C_l at $\alpha \approx 8°$. Similar results have been obtained by Althaus (1980) and shown in Figure 26. Althaus used a strain gauge balance arrangement to measure lift and a wake rake to measure drag. A drawback of using a wake rake will be addressed later. Althaus did observe a small hysteresis loop at low Reynolds numbers. No apparent hysteresis was observed in the current study.

The sharp rise in C_l at low Reynolds numbers is believed to be the result of a laminar separation bubble on the upper surface of the wing. O'Meara and Mueller (1987) showed that the length of the separation bubble tends to increase with a reduction in Re_c. A reduction in the turbulence intensity also tends to increase the length of the bubble. The lift-curve slope is affected by separation bubbles. A longer bubble is usually associated with a decrease in the lift-curve slope (Bastedo and Mueller, 1985). This is the kind of behavior observed with the Eppler 61 airfoil in this investigation. Flow visualization by Mueller and Burns (1982) showed the presence of a separation bubble on the Eppler 61 airfoil at $Re_c = 46,000$.

In the water tunnel, the turbulence intensity is larger than in the wind tunnel. Therefore, the smaller C_{l_α} and sharp rise in C_l observed in the wind tunnel for $2° \leq \alpha \leq 8°$ might not be present at all in the water tunnel data for the same Reynolds numbers. This is exactly

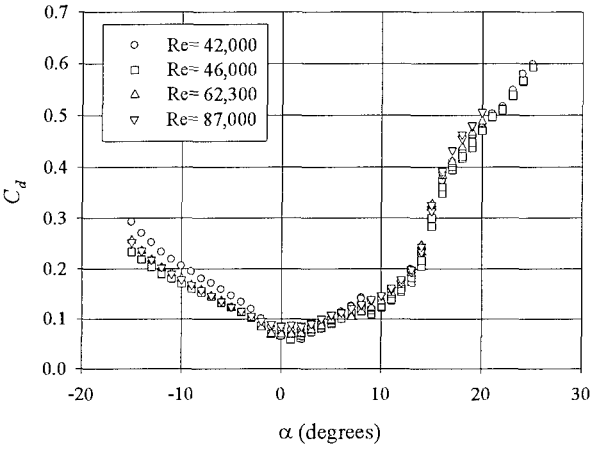

Figure 25: 2D drag coefficient on the Eppler 61 airfoil in the wind tunnel with UND-FB2

what happened for $Re_c = 42,000$ and $Re_c = 46,000$, as shown in Figure 27. The drag coefficient appears to be less affected, within the uncertainty of the measurements. Figure 28 shows the C_d curves obtained in the water tunnel for the Eppler 61 airfoil.

Figures 29 through 31 show comparisons of the current Eppler 61 results with published data. There is, in general, a good agreement between the current data and published data. The most significant difference is in the stall angle; there appears to be a 2° difference in α_{stall}.

Measurement uncertainty with UND-FB2

Uncertainties in the measurements were computed using the Kline-McClintock technique (Kline and McClintock, 1953) for error propagation. As indicated earlier, the two main sources of uncertainty were the quantization error and the uncertainty arising from the standard deviation of a given mean output voltage. The quantiza-

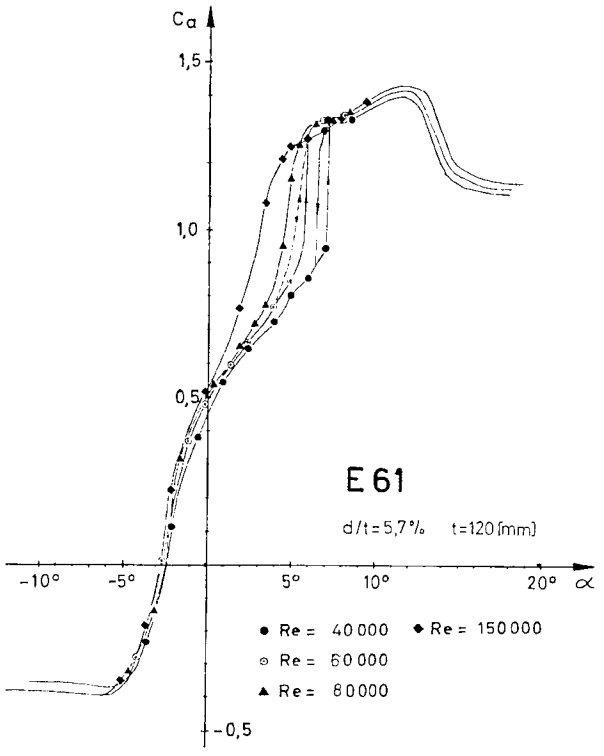

Figure 26: Althaus' results for 2D lift coefficient on the Eppler 61 airfoil (Althaus, 1980)

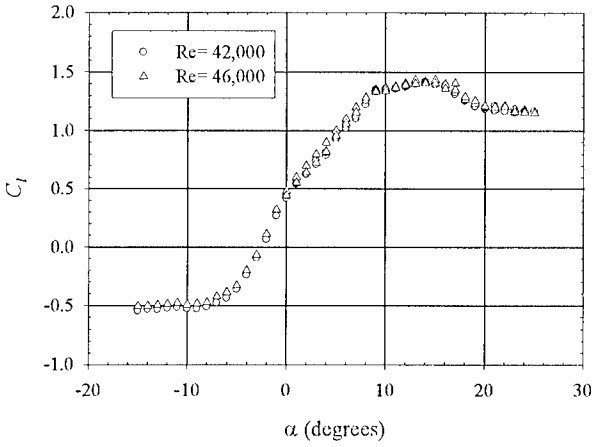

Figure 27: 2D lift coefficient on the Eppler 61 airfoil in the water tunnel with UND-FB2

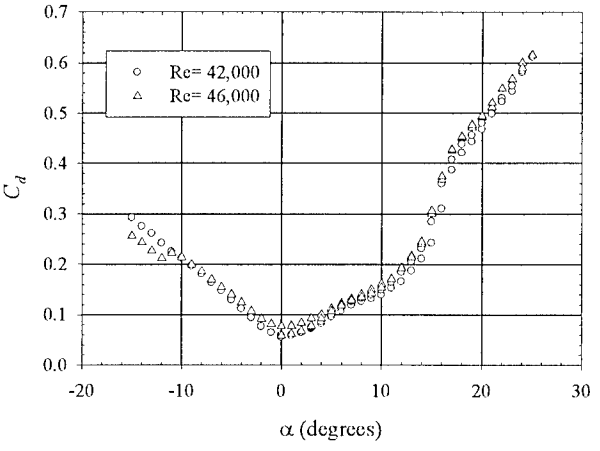

Figure 28: 2D drag coefficient on the Eppler 61 airfoil in the water tunnel with UND-FB2

tion error, described earlier, was smaller with the NIDAQ card than with the UEI card due to the better resolution of the A/D converter (16 bits compared to 12 bits). The uncertainty in the angle of attack was determined to be on the order of $0.2° - 0.3°$. The error from the encoder was negligible. The encoder offered an excellent resolution of 2,000 counts per degree, which gave an uncertainty of 5×10^{-4}. Figures 32 and 33 show a comparison of wind tunnel and water tunnel results for the Eppler 61 airfoil at $Re_c = 42,000$. Error bars indicate the uncertainty in C_l and C_d when the NIDAQ card is used. The average uncertainties for C_l and C_d in the range of angles of attack tested are approximately 4% in the water tunnel and 6% in the wind tunnel.

The new balance in itself is also more sensitive than the old balance. This allows experiments at smaller velocities in the water tunnel. As of now, results with different wings have shown a high degree of repeatability for Reynolds numbers as low as $40,000$. A major challenge in measurements at Reynolds numbers below $40,000$ is being able to measure drag accurately. At $Re_c = 20,000$, the minimum drag can be as low as $0.02\,N$, which corresponds to a load of approximately 2 grams. A fine drag calibration of the balance showed that 1 gram was sufficient to deflect the drag flexure and yield a reasonable output voltage. However, this deflection is often on the order of signal noise.

Results for thin wings

This section will present results for thin flat and cambered wings. Some additional issues associated with determining aerodynamic characteristics as a function of Reynolds numbers will also be addressed. Accurate measurements of C_l and C_d with endplates and small aspect-ratio models are difficult to obtain at low Reynolds numbers because of the interaction between the thick boundary layers on the endplates and the flow around the wing, which results into a three-dimensional flow along the span of the model. This must be kept in mind when examining the following results.

Flat-plate wings

Some results for the flat-plate models (two endplates for 2D tests and one endplate for semi aspect-ratio tests)

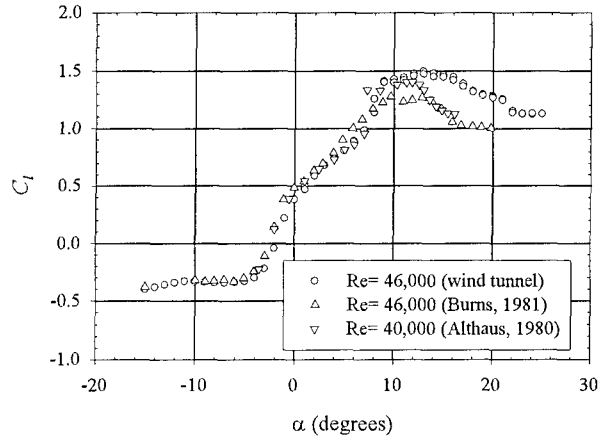

Figure 29: Comparison of 2D lift coefficient on the Eppler 61 airfoil and published data with UND-FB2

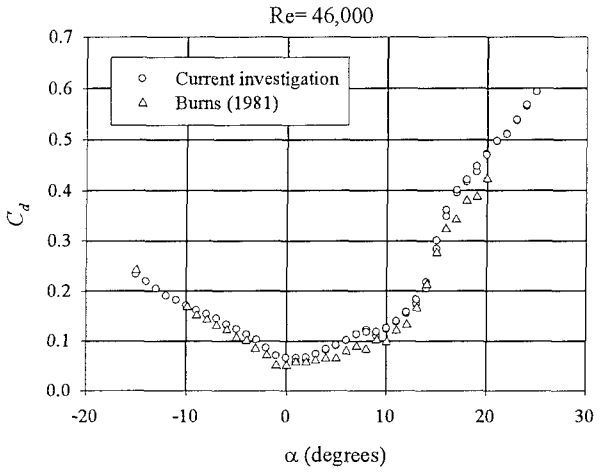

Figure 30: Comparison of 2D drag coefficient on the Eppler 61 airfoil and published data with UND-FB2

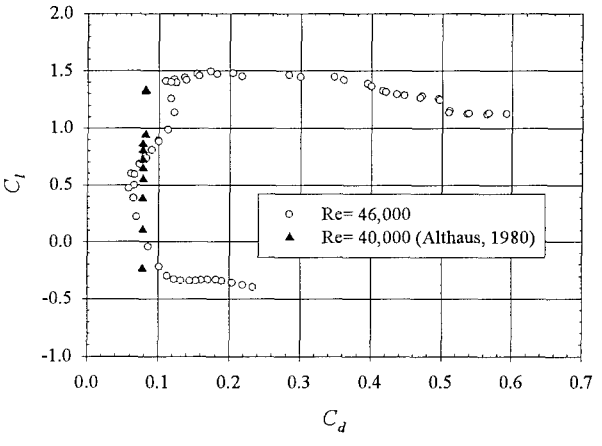

Figure 31: Comparison of 2D drag polar for the Eppler 61 airfoil and published data with UND-FB2

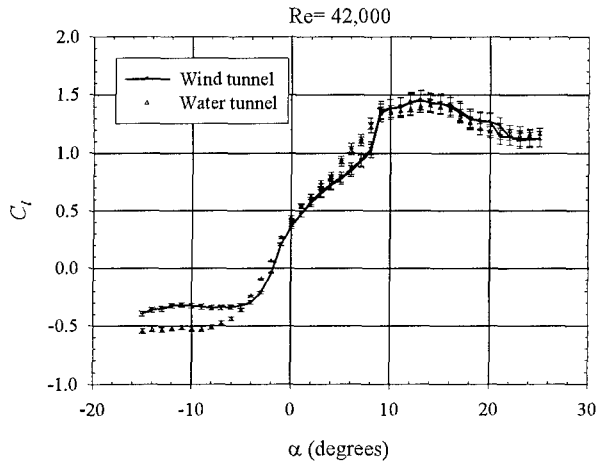

Figure 32: Comparison of the 2D lift coefficient on the Eppler 61 airfoil in wind and water tunnels with UND-FB2

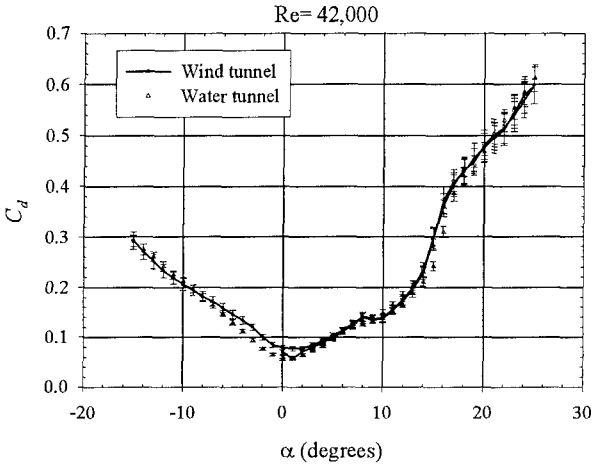

Figure 33: Comparison of the 2D drag coefficient on the Eppler 61 airfoil in wind and water tunnels with UND-FB2

can be seen in Figures 34 through 39 for $Re_c = 80,000$ and $Re_c = 140,000$. Figures 34 and 37 show a significant reduction in the lift-curve slope C_{L_α} for semi-infinite wings.

The lift-curve slope values obtained from the wind tunnel data are compared to theoretical values for thin wings of different semi-span aspect ratios in Figure 40. Equation 1 from Anderson (1991) was used to estimate the theoretical values of C_{L_α}:

$$C_{L_\alpha} = a = \frac{a_0}{1 + \left(\frac{a_0 * 57.3}{\pi \mathrm{AR}}\right)(1+\tau)}, \qquad (1)$$

where a_0 is the 2D lift-curve slope in 1/degrees, AR is the aspect ratio of the full wing (AR $= 2 *$ sAR) and τ is the Glauert parameter (equivalent to an induced drag factor) varying typically between 0.05 and 0.25. The 2D value a_0 was determined to be $a_0 = 0.0938/\mathrm{deg}$. This corresponds to the average of all the slopes C_{L_α} (for all

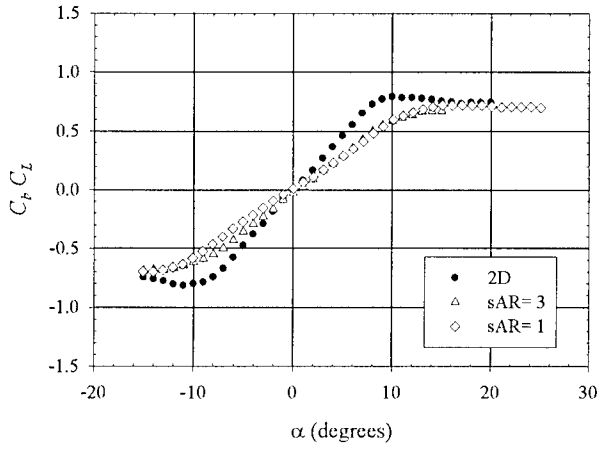

Figure 34: Lift coefficient on flat plates at $Re_c = 80,000$ with UND-FB1

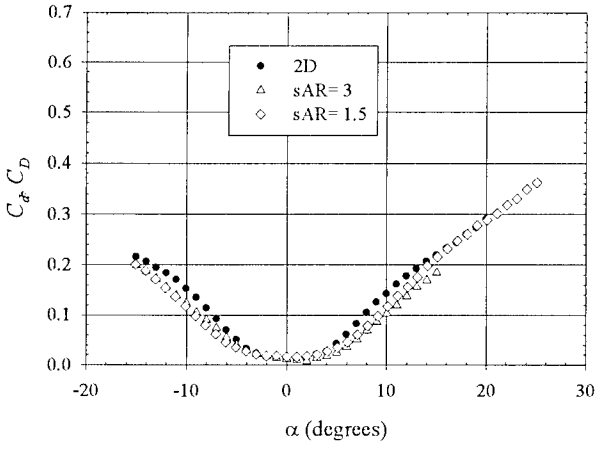

Figure 35: Drag coefficient on flat plates at $Re_c = 80,000$ with UND-FB1

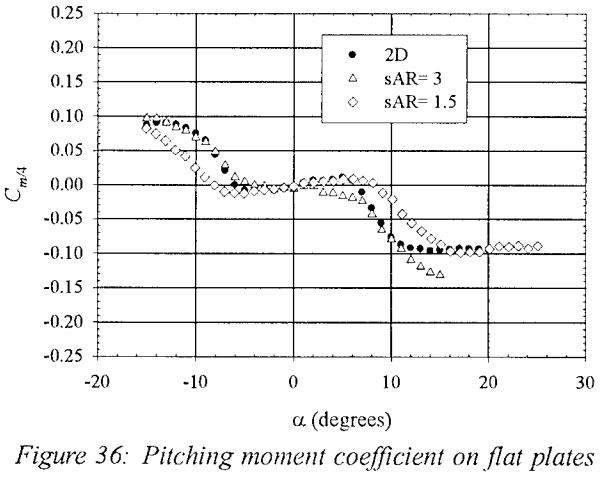

Figure 36: Pitching moment coefficient on flat plates at $Re_c = 80,000$ with UND-FB1

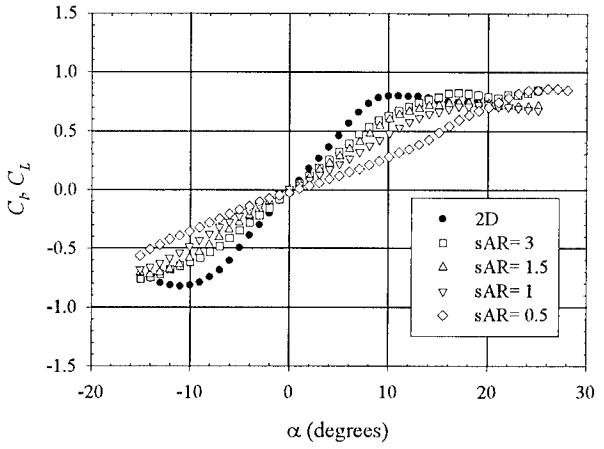

Figure 37: Lift coefficient on flat plates at $Re_c = 140,000$ with UND-FB1

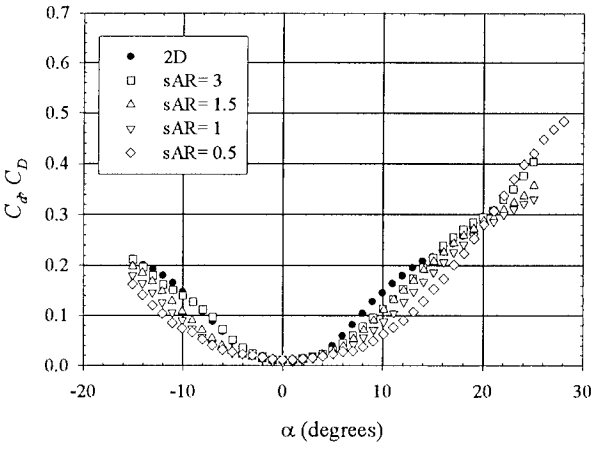

Figure 38: Drag coefficient on flat plates at $Re_c = 140,000$ with UND-FB1

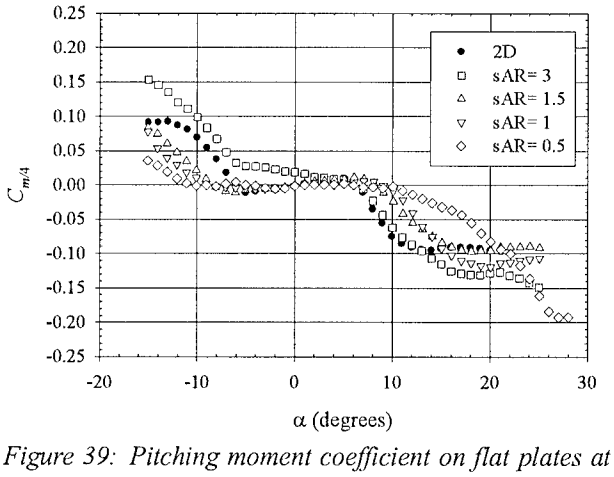

Figure 39: Pitching moment coefficient on flat plates at $Re_c = 140,000$ with UND-FB1

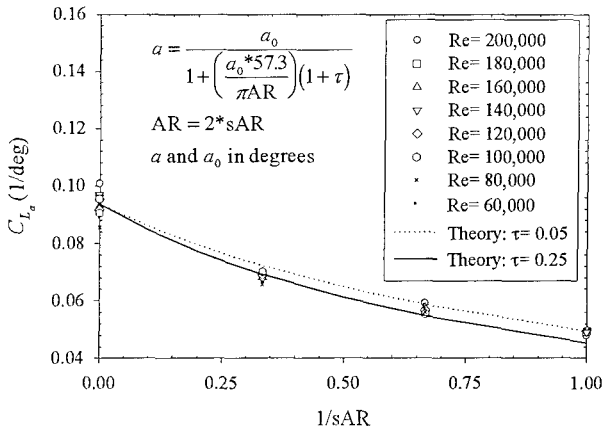

Figure 40: Lift-curve slope for flat-plate models in wind tunnel with UND-FB1

Reynolds numbers considered) for an infinite aspect ratio ($1/\text{sAR} = 0$). This value was picked instead of the conventional value of $a_0 = 2\pi/\text{rad} = 0.1/\text{deg}$ given by thin-airfoil theory. Figure 40 shows a very good agreement between the experimental values of C_{L_α} and the theoretical values estimated by Equation 1.

As the aspect ratio was decreased, Figures 34 and 37 also show that the linear region of the C_L vs α curve became longer and α_{stall} tended to increase. Moreover, both figures show that there was no abrupt stall for low aspect-ratio wings. For these low aspect ratios, C_L often reached a plateau and then remained relatively constant, or even started to increase, for increasing angles of attack.

Changing the aspect ratio of the models did not appear to have a measurable effect on the drag coefficient at $Re_c = 80,000$, as shown in Figure 35. At $Re_c = 140,000$, increasing the aspect ratio had the unexpected effect of increasing C_D for angles greater than 5°. No measurable difference was encountered in the range $-5° \leq \alpha \leq 5°$.

Finally, Figures 36 and 39 show the pitching moment at the quarter chord. Both figures indicate a slightly positive slope C_{m_α} around $\alpha = 0°$, even when considering the uncertainty. This would imply that the flat-plate models were statically unstable around $\alpha = 0°$. Increasing the Reynolds number from 80,000 to 140,000 tended to reduce the slope of $C_{m/4}$. The model with a semi-span aspect ratio of 3 indicated an irregular behavior at $Re_c = 140,000$ for $C_{m/4}$; the pitching moment was not zero at $\alpha = 0°$. This case will have to be repeated.

Aerodynamic characteristics as a function of Reynolds number: a different method

For tests without endplates, another balance arrangement, denoted arrangement number 3, was used and is presented in Figure 41. The lift and drag forces measured by the balance were for the wing-sting combination. The lift on the sting was basically zero. However, the drag of the sting alone, which dominated the total wing-sting drag, was not zero and was subtracted from the wing-sting values to get the C_D of the flat-plate wing alone.

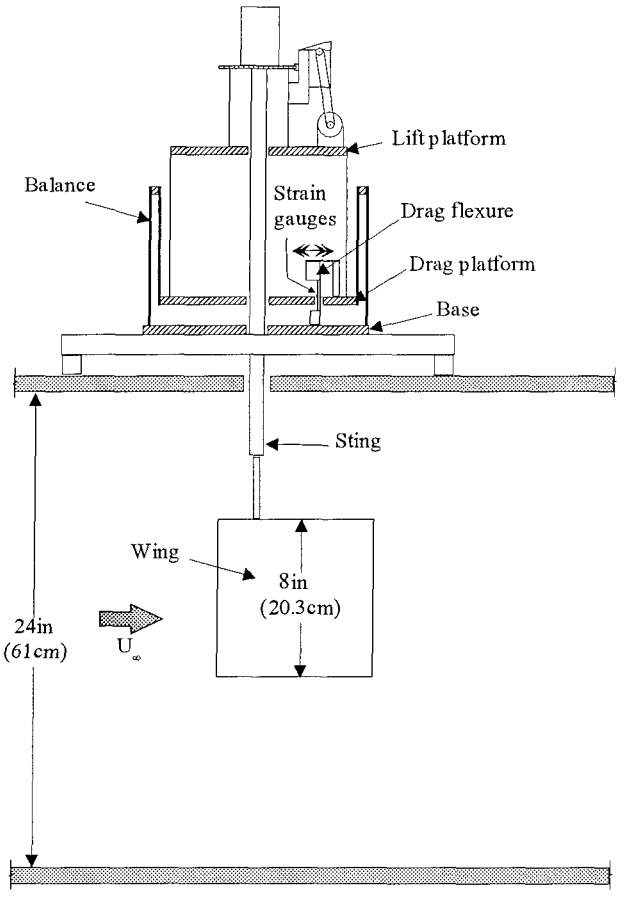

Figure 41: Balance arrangement (3) for finite wing tests with the new balance

In general, when investigators try to determine how $C_{L_{\max}}$ and $C_{D_{\min}}$ vary with Reynolds numbers, they determine $C_{L_{\max}}$ and $C_{D_{\min}}$ from C_L vs α and C_D vs α curves at different Reynolds numbers. It has been observed in this investigation that the values obtained do not always match the expected trend for drag because of the difficulty involved in measuring the very small drag forces. A slight offset in one C_L vs α or C_D vs α curve can lead to jagged $C_{L_{\max}}$ vs Re_c or $C_{D_{\min}}$ vs Re_c curves. A better technique was found to obtain $C_{D_{\min}}$ vs Re_c (the values of $C_{L_{\max}}$ vs Re_c are of lesser importance because micro-air vehicles will rarely fly at $C_{L_{\max}}$). For this technique, the angle of attack was fixed to the angle yielding the lowest C_D in a C_D vs α curve, and measurements were taken for a series of increasing and decreasing Reynolds numbers without stopping the tunnel. Results obtained with the new balance UND-FB2 using this technique on a finite wing of aspect ratio AR = 1 in the wind tunnel, presented in Figures 42 and 43, are promising and the trends obtained matched the expected reduction in $C_{D_{\min}}$ with increasing Reynolds numbers.

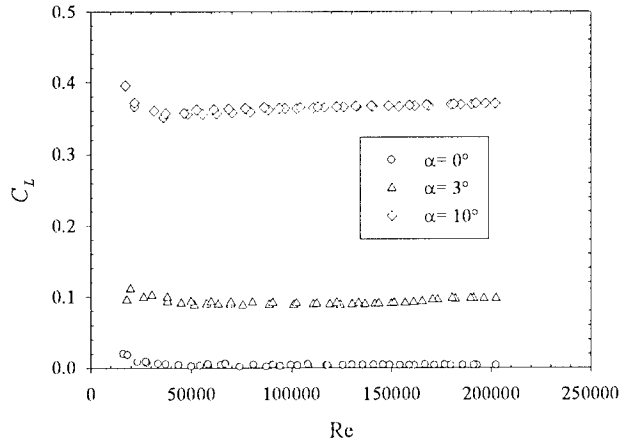

Figure 42: Lift coefficient variation with Re for AR $= 1$ *flat-plate wing with UND-FB2 (C8S8)*

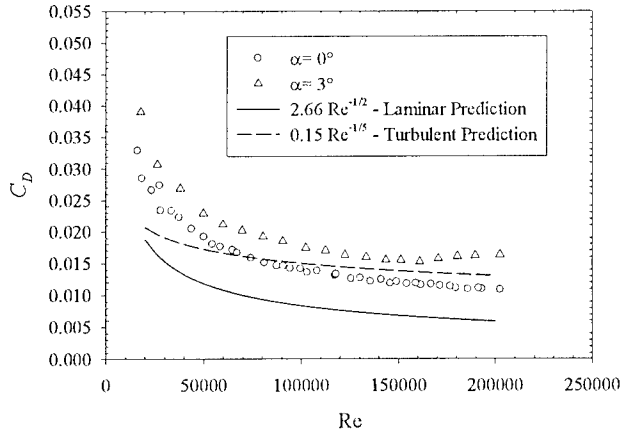

(a) $\alpha = 0°$ and $3°$

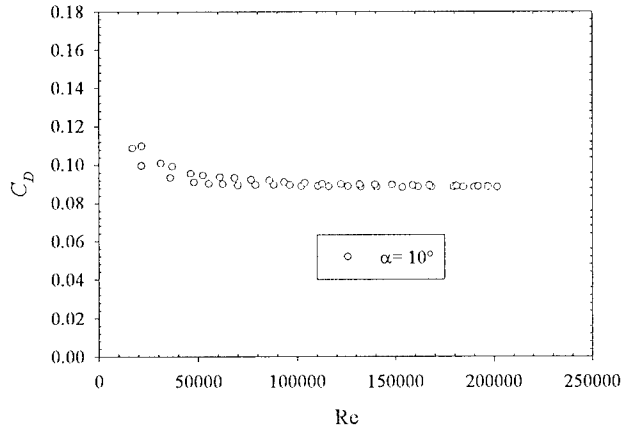

(b) $\alpha = 10°$

Figure 43: Drag coefficient variation with Re for AR $= 1$ *flat-plate wing with UND-FB2 (C8S8)*

Results at the angle of attack for $\left(\frac{L}{D}\right)_{\max}(\alpha \approx 3°)$ also show an increase in C_L and a decrease in C_D with increasing Reynolds number. The results of Figure 42 at $\alpha = 10°$ are smaller than the lift coefficient presented in Figure 34 for a model with sAR $= 1$ because of the lack of an endplate. For a given model, adding an endplate leads to an increase in lift compared to the case without an endplate, as shown in Figure 44. Adding one endplate did not have a significant effect on C_D, as shown in Figure 45. The wing used for this series of tests had a nominal chord $c = 8\,in$ and span $b = 12\,in$ [C8S12].

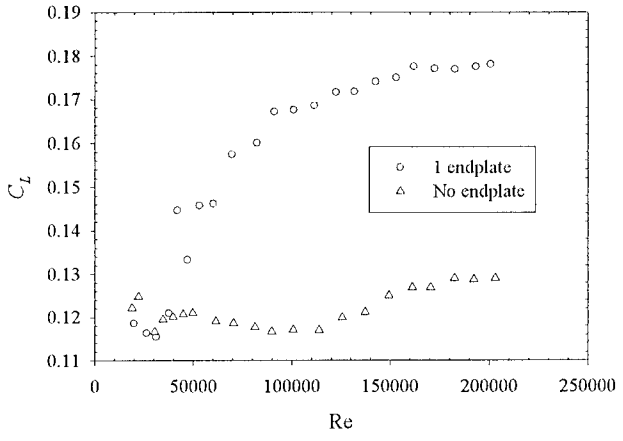

Figure 44: Lift coefficient variation with Re (C8S12) with UND-FB2 at $\alpha = 3°$

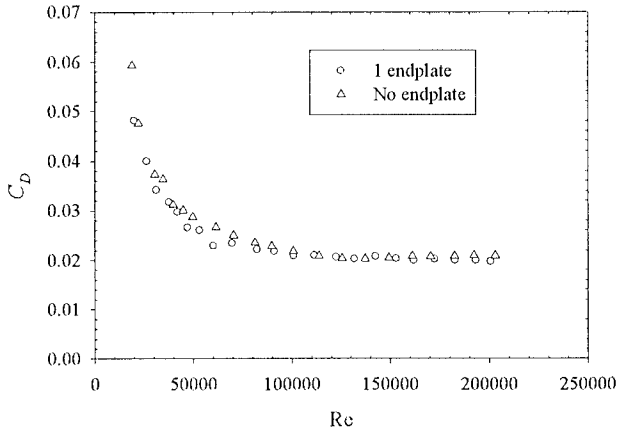

Figure 45: Drag coefficient variation with Re (C8S12) with UND-FB2 at $\alpha = 3°$

At an angle of attack $\alpha = 0°$, adding one or two endplates did not affect C_L for $Re_c > 60{,}000$; it remained basically around the expected value of zero, as shown in Figure 46. Moreover, adding endplates did not, once again, have a measurable effect on C_D, as presented in Figure 47. Since Figure 47 is for $\alpha = 0°$, it represents $C_{D_{\min}}$ versus Reynolds number for flat-plate wings. Experimental results are also compared to theory (Blasius: $C_{D_{\min}} = 2.66 Re^{-\frac{1}{2}}$) and CFD results in Figure 47. The

CFD results were computed by Greg Brooks (*Air Force Research Laboratory*, Wright-Patterson Air Force Base) using COBALT, a parallel, implicit, unstructured, finite volume laminar CFD code based on Godunov's exact Riemann method, developed by the *Air Force Research Laboratory* (see Strang, Tomaro and Grismer, 1999). All sets of data indicate the same trend. The experimental data was always larger than theory and the CFD results. This could have been caused by surface roughness, imperfect flow conditions, and so forth. Since all wind tunnel tests with the flat and cambered wings are usually conducted at Reynolds numbers greater than 60,000, the results presented in Figures 42 through 47 for $Re < 60,000$ should be analyzed with caution. The velocity in the wind tunnel is usually too low for $Re < 60,000$ to yield reliable results.

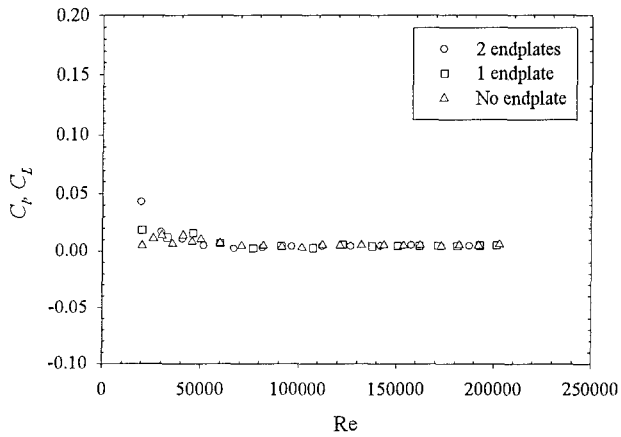

Figure 46: Lift coefficient variation with Re (C8S12) with UND-FB2 at $\alpha = 0°$

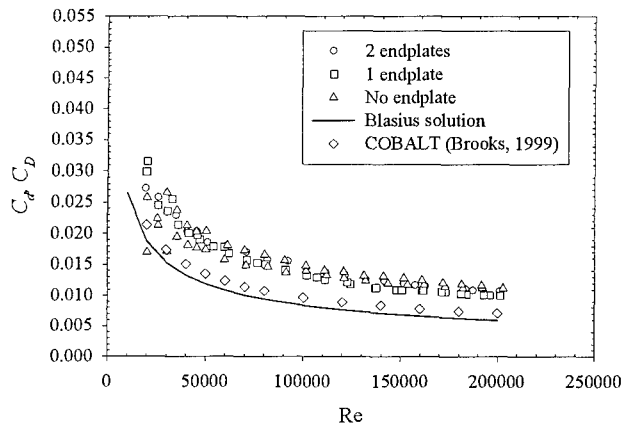

Figure 47: Drag coefficient variation with Re (C8S12) with UND-FB2 at $\alpha = 0°$

The results of Figure 47 seem to indicate that for thin flat-plate wings at $\alpha = 0°$ the drag coefficient acting on the wing is independent of aspect ratio. Results of Figure 47 were then compared to the drag coefficients

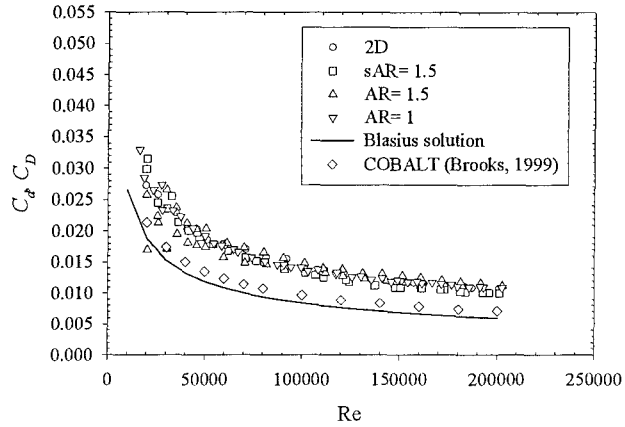

Figure 48: Minimum drag coefficient with Re for AR $\geq$ 1 flat-plate wings with UND-FB2

for the AR = 1 plate and no difference was obtained, as shown in Figure 48. For aspect ratios greater than one, the minimum drag coefficient is then independent of model size and the presence of endplates. For lower aspect ratios, preliminary tests indicated a larger $C_{D_{\min}}$. More work is in progress to fully understand the behavior of $C_{D_{\min}}$ as a function of Reynolds numbers for the very low aspect-ratio wings (AR < 1). Similar tests will also have to be conducted on the cambered wings. The non-measurable difference in $C_{D_{\min}}$ with Reynolds numbers might just be valid for flat-plate wings. Adding camber might change the results. Preliminary results seem to indicate this trend.

Cambered-plate wings

Results were also obtained for cambered-plate models using the balance arrangement with one or two endplates (semi-infinite or 2D tests). In general, camber led to better aerodynamic characteristics due to an increase in lift, even though drag also increased. Figures 49 through 54 show some results for the cambered plates at $Re_c = 60,000$ and $Re_c = 140,000$. With cambered plates, $C_{D_{\min}}$ was slightly larger than for flat plates. The maximum lift coefficient was also larger, as expected. Moreover, the variation in C_L with angle of attack at small angles was less linear for cambered plates than for flat plates. Finally, the behavior of the moment coefficient $C_{m/4}$ for the cambered plates was very different than the behavior with the flat plates. A rise in $C_{m/4}$ occurred after $\alpha \approx 5°$, leading to a hump at around $\alpha \approx 10°$. This was not observed with the flat plates. Flow visualization will hopefully explain this behavior.

Equation 1 was also used to compare the experimental values of C_{L_α} at $\alpha_{C_L=0}$ for the cambered plates to theoretical values. The 2D value a_0 used was $a_0 = 0.1097/\text{deg}$. Figure 55 shows a good agreement between theory and experiments.

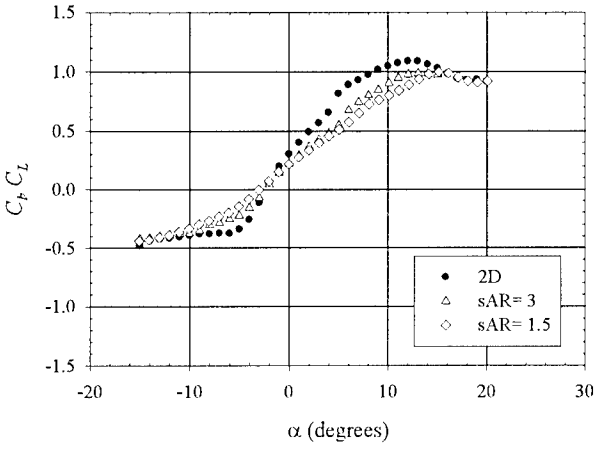

Figure 49: Lift coefficient on cambered plates at $Re_c = 60,000$ with UND-FB1

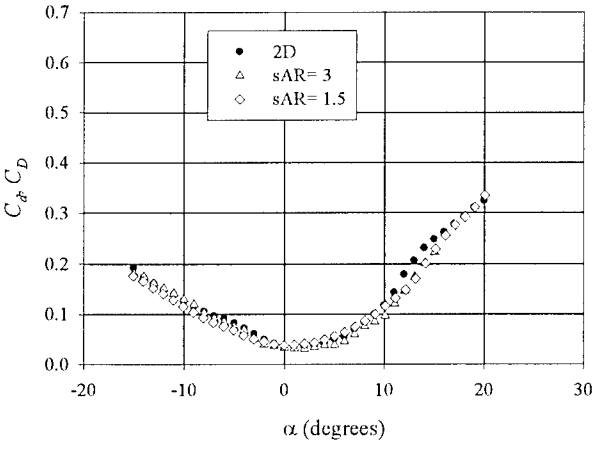

Figure 50: Drag coefficient on cambered plates at $Re_c = 60,000$ with UND-FB1

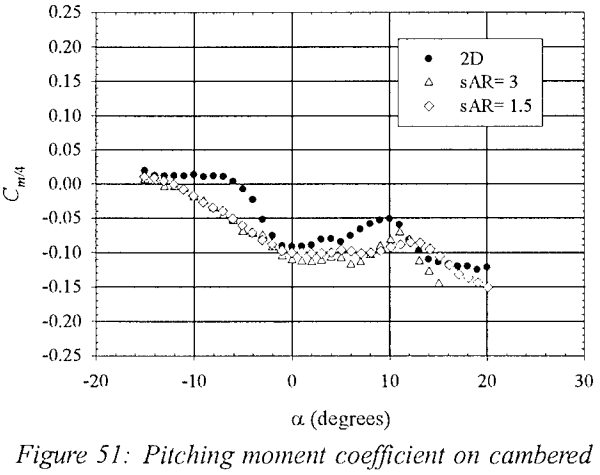

Figure 51: Pitching moment coefficient on cambered plates at $Re_c = 60,000$ with UND-FB1

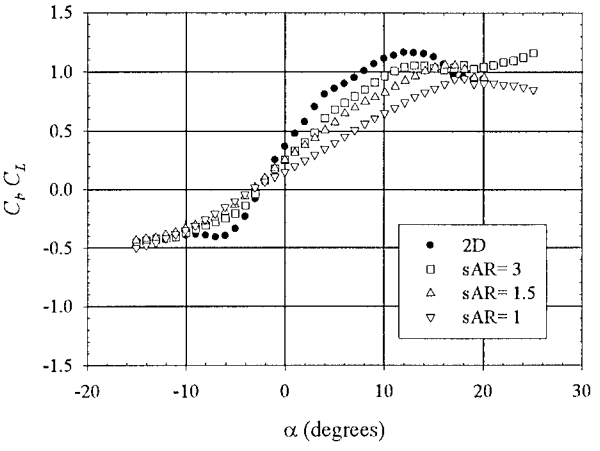

Figure 52: Lift coefficient on cambered plates at $Re_c = 140,000$ with UND-FB1

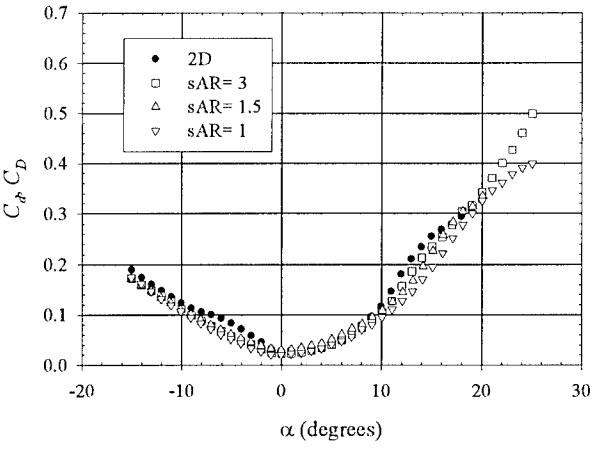

Figure 53: Drag coefficient on cambered plates at $Re_c = 140,000$ with UND-FB1

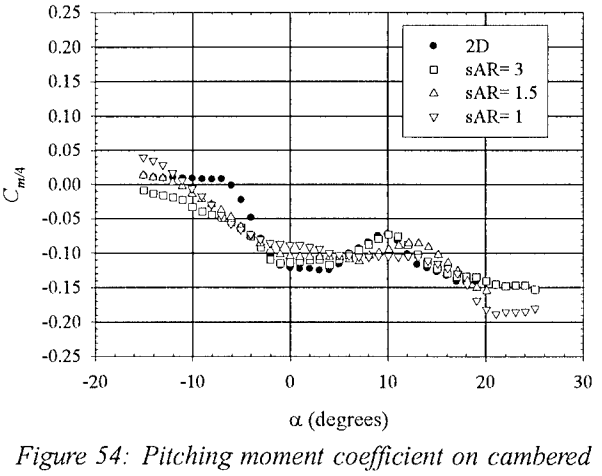

Figure 54: Pitching moment coefficient on cambered plates at $Re_c = 140,000$ with UND-FB1

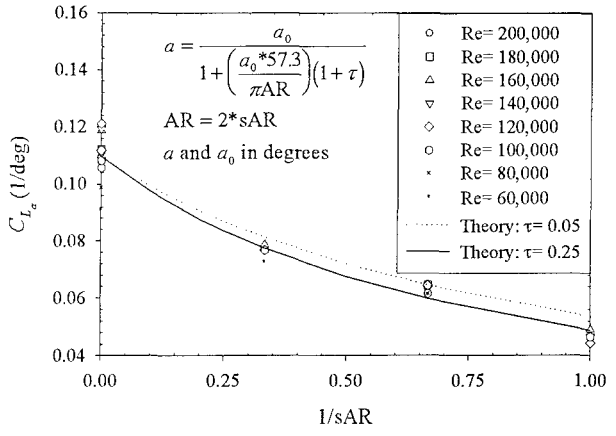

Figure 55: Lift-curve slope for cambered-plate models in wind tunnel with UND-FB1

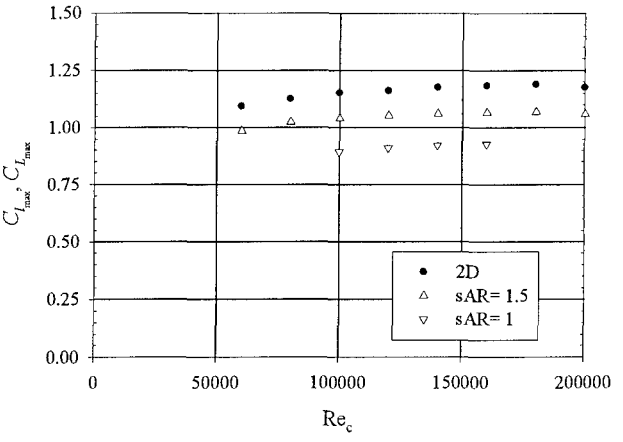

Figure 56: Maximum lift coefficient as a function of Re_c for cambered wings with UND-FB1

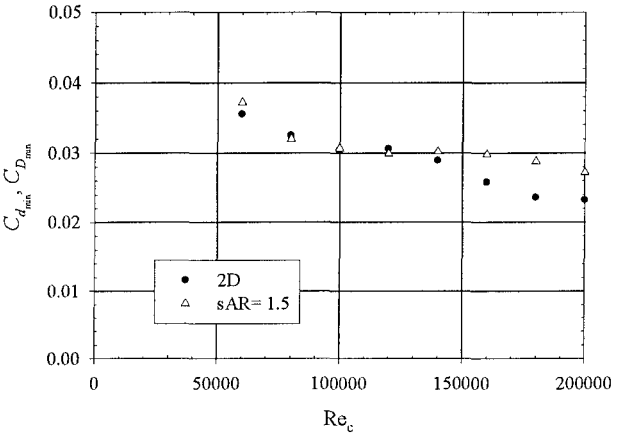

Figure 57: Minimum drag coefficient as a function of Re_c for cambered wings with UND-FB1

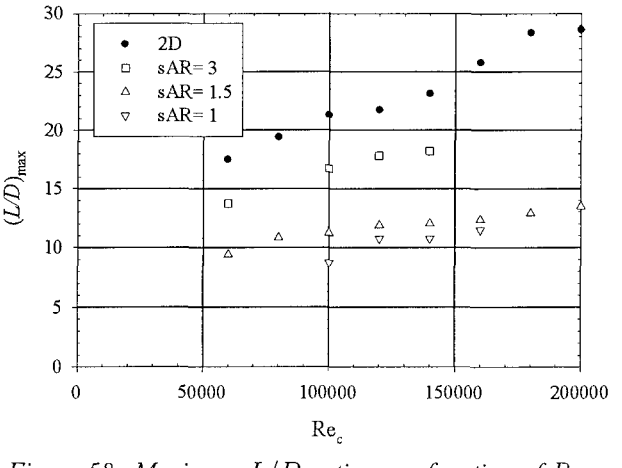

Figure 58: Maximum L/D ratio as a function of Re_c for cambered wings with UND-FB1

Since the cambered wings showed better aerodynamic characteristics, and hence are more suitable in the design of micro-air vehicles, only performance data for the cambered plates is presented. Figures 56 through 59 show the behavior of $C_{L_{max}}$, $C_{D_{min}}$, $\left(\frac{L}{D}\right)_{max}$ and $\left(\frac{C_L^{3/2}}{C_D}\right)_{max}$ as a function of Reynolds number. The maximum L/D ratio is related to the maximum range for a propeller driven airplane, while the maximum $C_L^{3/2}/C_D$ is related to best endurance (longest flying time possible). As expected, $C_{L_{max}}$ increased with Reynolds number and aspect ratio in the range of Reynolds numbers tested. The same expected behavior was obtained for $\left(\frac{L}{D}\right)_{max}$ and $\left(\frac{C_L^{3/2}}{C_D}\right)_{max}$. On the other hand, $C_{D_{min}}$ showed an increase with decreasing Reynolds number, as was also expected. The maximum L/D generally occurred at $\alpha = 3°$ to $4°$, while $\left(\frac{C_L^{3/2}}{C_D}\right)_{max}$ occurred at $\alpha = 4°$ to $5°$. It is important to remember that the endplates have been shown to have an effect on the lift coefficients of flat-plate wings, and probably cambered-plate wings also. As mentioned earlier, the effect of the endplates on the drag characteristics of cambered-plate wings is still under investigation. The results presented in this report must then be analyzed with the possible effect of the endplates in mind; the numerical values should not be taken as the ultimate results. The effect of the endplates on the pitching moment has not been investigated for both flat-plate and cambered-plate wings.

Effect of trailing-edge geometry

Four models [$c = 8\,in$ ($c = 20.3\,cm$) and $b = 12\,in$ ($b = 30.5\,cm$)] were tested in the wind tunnel at several chord Reynolds numbers to see if the trailing-edge geometry had any influence on the aerodynamic characteristics of flat plates and cambered plates at low chord

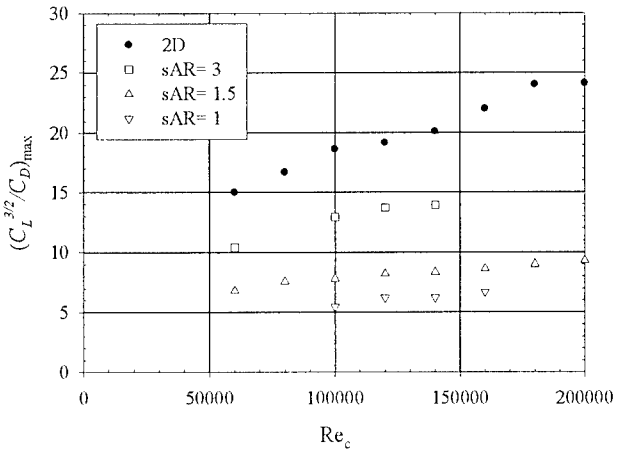

Figure 59: Maximum $C_L^{3/2}/C_D$ ratio as a function of Re_c for cambered wings with UND-FB1

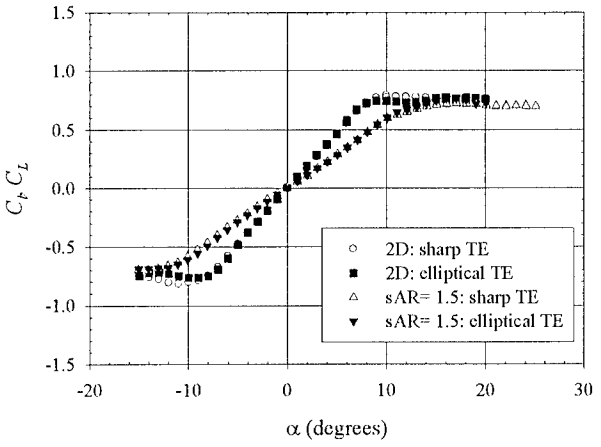

Figure 60: Trailing-edge geometry effect on lift coefficient at $Re_c = 80,000$ on flat plates in the wind tunnel with UND-FB1

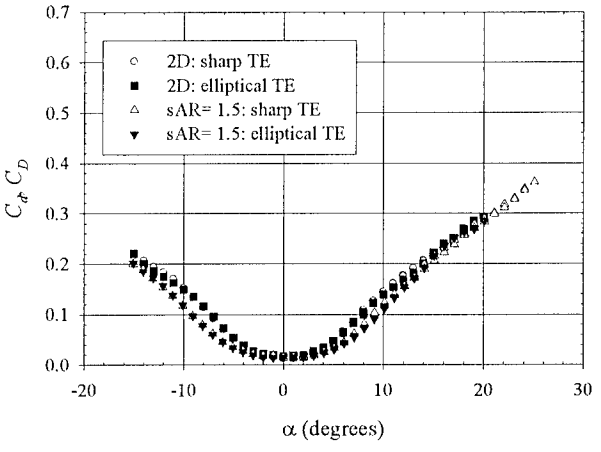

Figure 61: Trailing-edge geometry effect on drag coefficient at $Re_c = 80,000$ on flat plates in the wind tunnel with UND-FB1

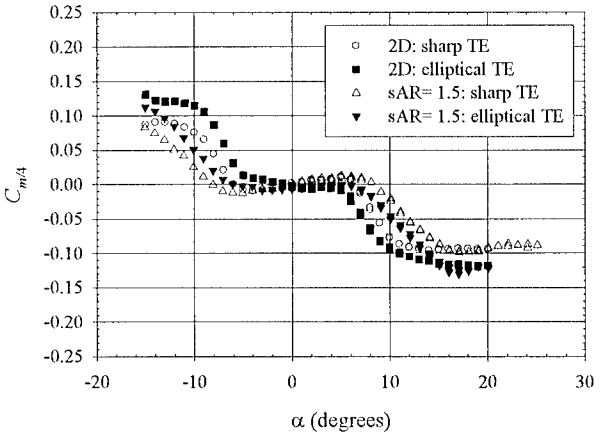

Figure 62: Trailing-edge geometry effect on pitching moment coefficient at $Re_c = 80,000$ on flat plates in the wind tunnel with UND-FB1

Reynolds numbers. The first two models had a tapered trailing edge, while the other two models had an elliptical trailing edge. Results were obtained for infinite models (2D case) and models with a semi-span aspect ratio sAR $= 1.5$. For both cases, no significant difference was observed in C_L or C_l, and C_D or C_d, as a function of trailing-edge geometry, as shown in Figures 60 and 61 for $Re_c = 80,000$. A difference was however observed in the moment coefficient $C_{m/4}$. For a sharp trailing edge, C_{m_α} often appeared to be positive around $\alpha = 0°$, even with the uncertainty considered (error bars in $C_{m/4}$ are about the size of the symbols). With the elliptical trailing edge, the 2D cases at $Re_c = 80,000$ showed a stable negative value of C_{m_α}, as shown in Figure 62. For a semi-span aspect ratio of 1.5, C_{m_α} was basically zero at $\alpha = 0°$. Flow visualization to be performed later may explain this phenomenon.

With the cambered plates, there was basically no difference between a sharp trailing edge and an elliptical trailing edge at $Re_c = 80,000$, as shown in Figures 63 through 65. Results with the cambered plates seem to agree with Laitone (Laitone, 1996 and 1997), who showed that at low Reynolds numbers, a sharp trailing edge is not as critical as for larger Reynolds numbers.

The influence of the leading-edge geometry was also investigated by looking at the lift and drag characteristics of a flat-plate model in 2D and sAR $= 1.5$ configurations in the water tunnel at $Re_c = 39,000$ and $Re_c = 60,000$. For these tests, the existing C8S12 model was rotated 180 degrees (tapered leading edge and elliptical trailing edge). No difference was noticed in the results for lift and drag. Laitone (1996 and 1997) did notice a significant increase in lift at $Re_c = 20,700$ for a *thicker* reversed NACA 0012 airfoil (the sharp trailing edge was facing the flow). Further tests will be conducted in the wind tunnel at larger Reynolds numbers on flat-plate and cambered-plate wings to complete this study of the leading-edge geometry effect

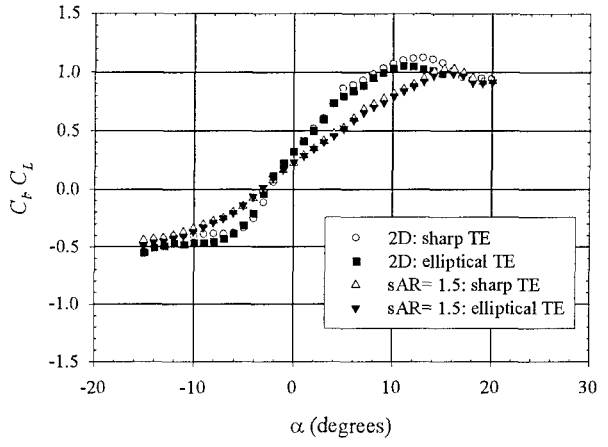

Figure 63: Trailing-edge geometry effect on lift coefficient at $Re_c = 80,000$ on cambered plates in the wind tunnel with UND-FB1

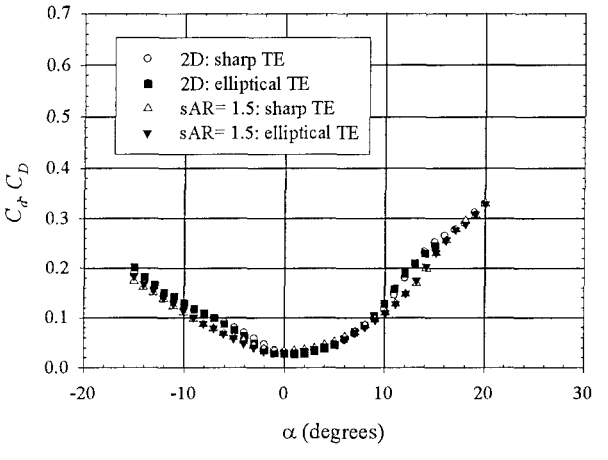

Figure 64: Trailing-edge geometry effect on drag coefficient at $Re_c = 80,000$ on cambered plates in the wind tunnel with UND-FB1

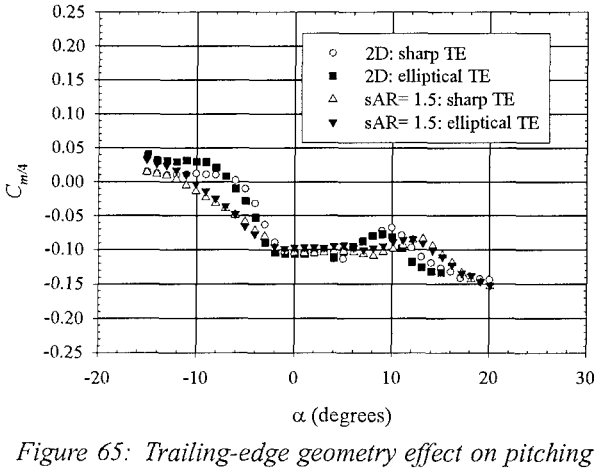

Figure 65: Trailing-edge geometry effect on pitching moment coefficient at $Re_c = 80,000$ on cambered plates in the wind tunnel with UND-FB1

on the aerodynamic characteristics of thin wings/airfoils.

Effect of freestream turbulence

Mueller et al. (1983) showed that an increase in freestream turbulence intensity reduced the minimum drag acting on an 11% thick Lissaman 7769 airfoil at $Re_c = 150,000$ and slightly increased $C_{l_{\max}}$. This was caused by an earlier laminar shear layer transition, hence earlier flow reattachment (i.e., a shorter separation bubble), with a larger turbulence intensity. At large angles of attack where the flow is mostly separated, they observed an increase in drag coefficient with an increase in turbulence intensity. Increasing the turbulence intensity also helped to eliminate some of the hysteresis encountered in C_l and C_d for that particular airfoil.

Pohlen (1983) also looked at the influence of turbulence intensity on a 13% thick Miley airfoil (M06-13-128) (see Miley, 1972). He found that increasing the turbulence intensity helped to reduce the hysteresis in C_l and C_d and slightly improved airfoil performance.

Tests were then conducted in the wind tunnel with different screens upstream of the flat-plate sAR $= 1.5$ models and a flow restrictor downstream of the model to see if a difference in the turbulence intensity could result in different aerodynamic properties for the models used in this investigation. The flow restrictor, or strawbox, was made of drinking straws packed in a wooden frame and placed between the test section and the diffuser. The additional turbulence intensity generated by the strawbox was determined to be approximately 0.05% (Brendel and Huber, 1984). Table 3 indicates the mesh size and nominal freestream turbulence intensity in the test section with only a screen present (no flow restrictor).

Screen	Mesh size (meshes/cm)	Wire diameter (mm)	Turbulence %
Fine	7.09	0.245	0.25
Medium	3.15	0.508	0.45
Coarse	0.64	1.397	1.3

Table 3: Turbulence screen data (Pohlen, 1983; and Brendel and Huber, 1984)

No measurable differences were observed in the results for different turbulence intensities at $Re_c = 60,000$ on the sAR $= 1.5$ flat-plate model, as shown in Figures 66 and 67. Only a slight increase in $C_{L_{\max}}$ and an increase in C_D for large angles of attack was noticed for the case with the fine mesh and with the strawbox. All other cases gave the same results. Therefore, the effect of turbulence intensity appeared to be minimal in the wind tunnel for the models tested. Similar results were

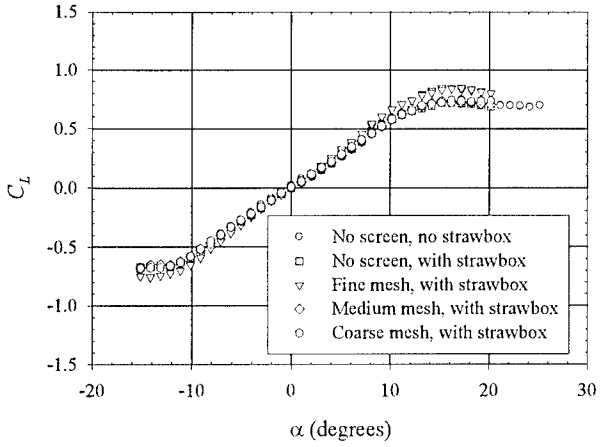

Figure 66: Freestream turbulence effect on lift coefficient at $Re_c = 60,000$ in the wind tunnel for the sAR $= 1.5$ *flat-plate model with UND-FB1*

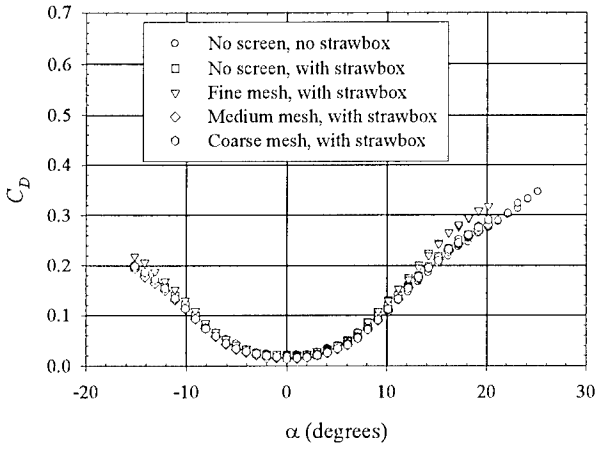

Figure 67: Freestream turbulence effect on drag coefficient at $Re_c = 60,000$ in the wind tunnel for the sAR $= 1.5$ *flat-plate model with UND-FB1*

obtained at $Re_c = 120,000$ in the wind tunnel, and at $Re_c = 39,000$ and $Re_c = 60,000$ in the water tunnel.

Effect of endplates on 2D measurements

It has been shown in previous experiments at Notre Dame that the presence of the endplates during 2D tests usually leads to a larger $C_{D_{\min}}$. For an 18% thick airfoil (NACA $66_3 - 018$), Mueller and Jansen (1982) showed that the interaction between the endplates and the model resulted in a 20% increase in $C_{d_{\min}}$ at Reynolds numbers between 60,000 and 200,000.

Since most of the tests in the current investigation were conducted at very low speeds, the interaction between the boundary layer growing on the endplates and the wing created a *corner* flow, as depicted in Figure 68, which acted over a significant portion of the wing span and significantly altered the 2-dimensionality of the

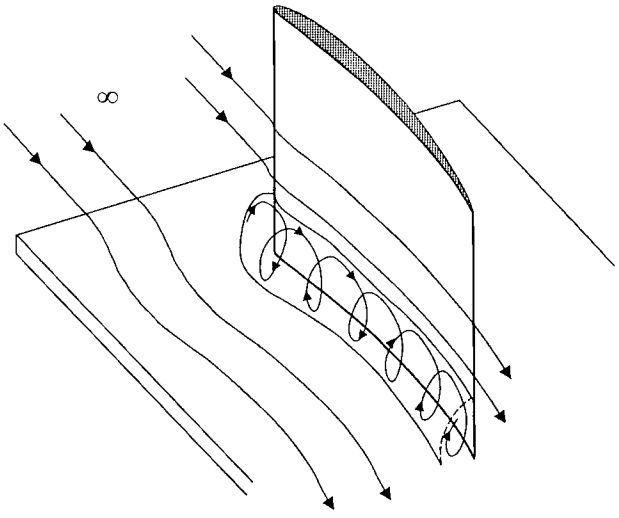

Figure 68: Schematic of corner flow on wing

flow over the wing. This phenomenon of the corner flow has been investigated by several authors, including Hawthorne (1954) and Barber (1978) who looked at the flow around struts near a wall.

In order to verify the effect of the endplates on the aerodynamic characteristics of the Eppler 61 airfoil, a 3-piece Eppler 61 model was used. With this setup, a section of an Eppler 61 model was free to move between two other sections of the same airfoil. These two other sections were fixed to the endplates in the wind tunnel, as shown in Figure 69, at the same angle of attack as the middle section. A small gap was present between the end models and the center piece connected to the force balance. Figure 70 shows the three pieces of the 3-piece Eppler 61 model.

The angle of attack of the 3-piece Eppler 61 model was adjusted to a certain value and the velocity in the tunnel, hence the Reynolds number, was varied. The behavior of C_d and C_l was measured. From the previous 2D results on the Eppler 61 airfoil, it was determined that $C_{d_{\min}}$ occurred at $\alpha = 0°$ and the angle for zero lift was about $\alpha = -2°$. The behavior of C_d vs Re_c was first obtained at these two angles of attack. Figures 71 and 72 show that the drag coefficient with the 3-piece Eppler 61 model was much smaller than with the full model. This result is similar to that reported by Mueller and Jansen (1982) for the NACA $66_3 - 018$ airfoil. The lift coefficient with the 3-piece model was higher than with the full model. The aerodynamic characteristics with the 3-piece model were closer to true 2-dimensional results, where a larger C_l and smaller C_d would normally be expected. The behavior of C_l and C_d with Reynolds numbers also followed the expected trends. A reduction in C_d and an increase in C_l were observed with increasing Reynolds numbers. Results from Althaus (1980) and de Vries et al. (1980) are also included in the figures for comparison. As was mentioned earlier for Althaus,

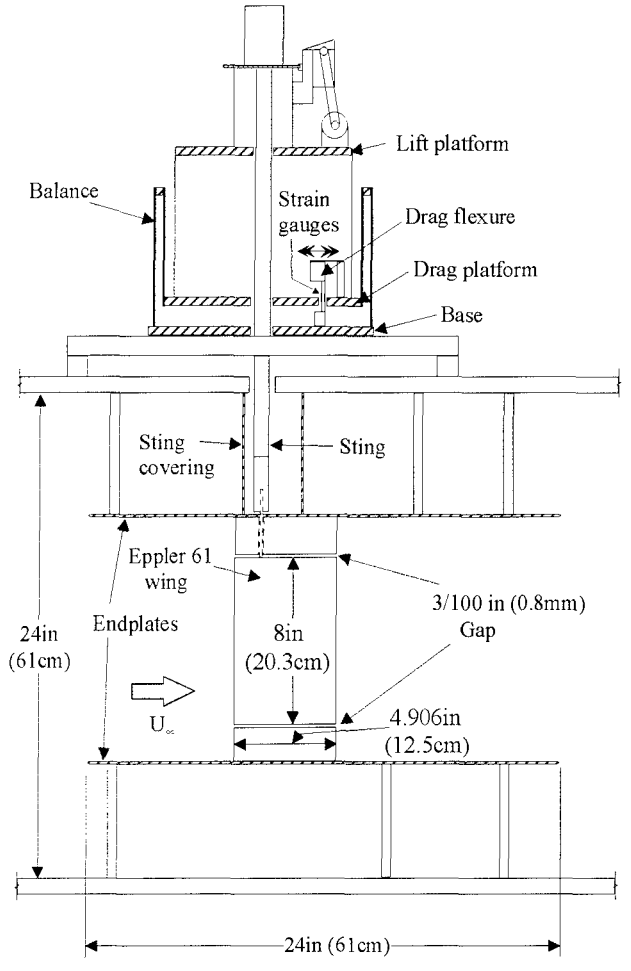

Figure 69: New-balance arrangement for 3-piece Eppler 61 airfoil tests in wind tunnel

these investigators used a strain gauge force balance to measure lift and a wake rake to measure drag. Since the drag measured with a wake rake is usually obtained at the mid-span of the model, it does not take end effects, or 3D effects, into account. These end effects can be significant at very low Reynolds numbers. Therefore, drag coefficient results from Althaus and de Vries et al. were expected to be smaller than the present results and this trend was observed.

In order to study the effect of endplates at low Reynolds numbers, Selig et al. (1995) showed how C_d can vary for a two-dimensional airfoil along the span of the model at low Reynolds numbers. Figures 73 through 76 show drag polars on an SD6060 airfoil at $Re_c = 60,000$, $100,000$, $200,000$ and $300,000$, as obtained using a wake rake with the momentum technique for C_d and a strain gauge force balance for C_l. For $Re_c = 60,000$ and $Re_c = 100,000$, the drag polars varied significantly along the span of the model, which implied a three-dimensional flow. At $Re_c = 200,000$ and especially at $Re_c = 300,000$, the drag polars were relatively constant along the span and a nearly two-dimensional flow was believed to exist.

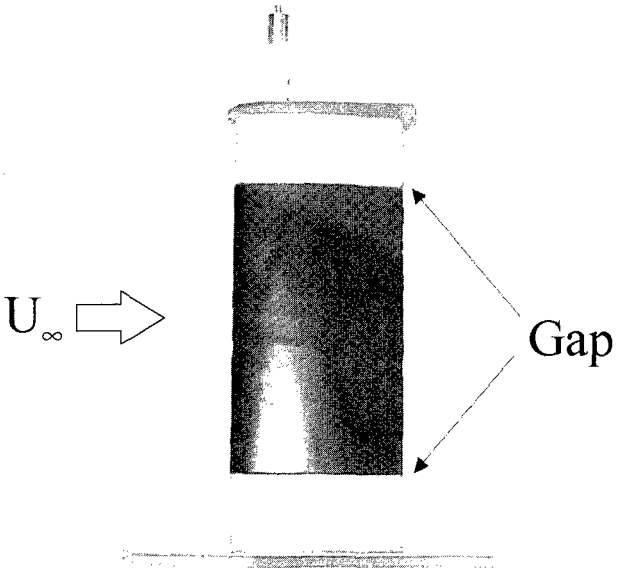

(a) Top view

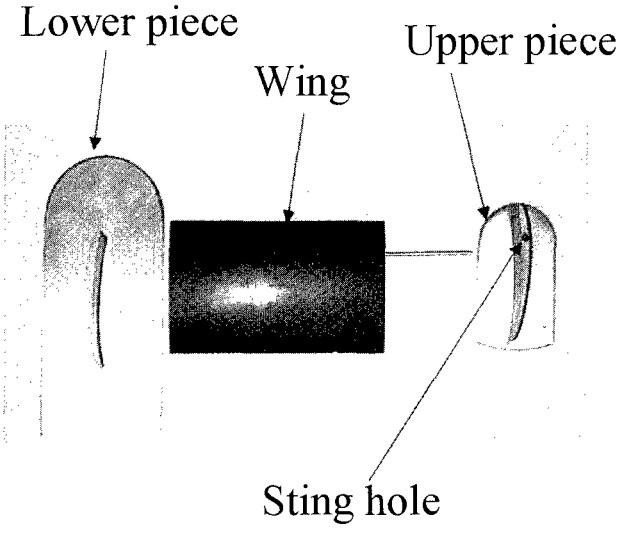

(b) Individual pieces

Figure 70: 3-piece Eppler 61 airfoil model tested in wind tunnel

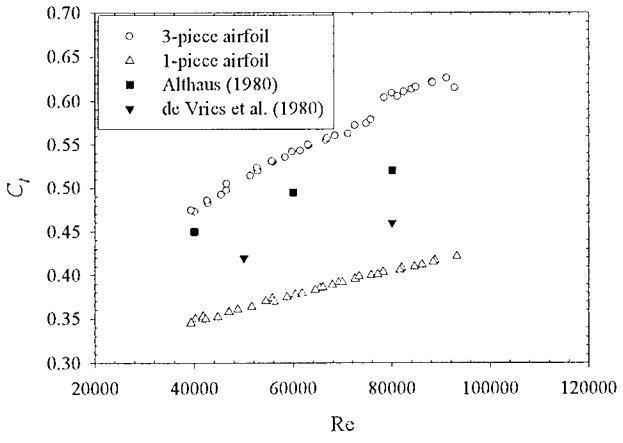

(a) Lift coefficient

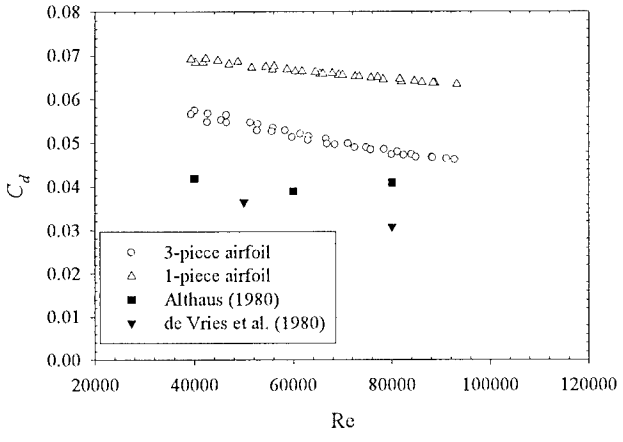

(b) Drag coefficient

Figure 71: Endplates effect on 2D characteristics of Eppler 61 airfoil at $\alpha = 0°$ with UND-FB2

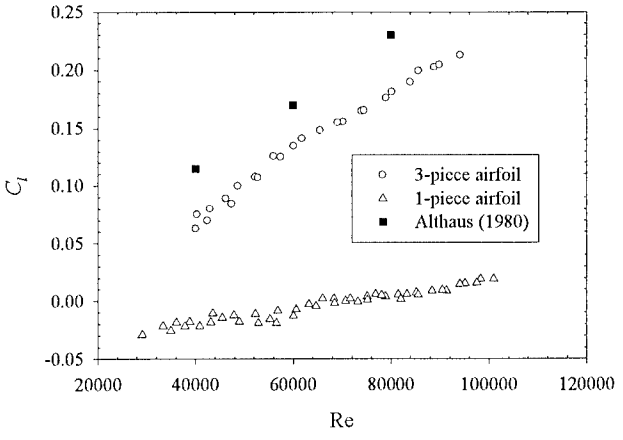

(a) Lift coefficient

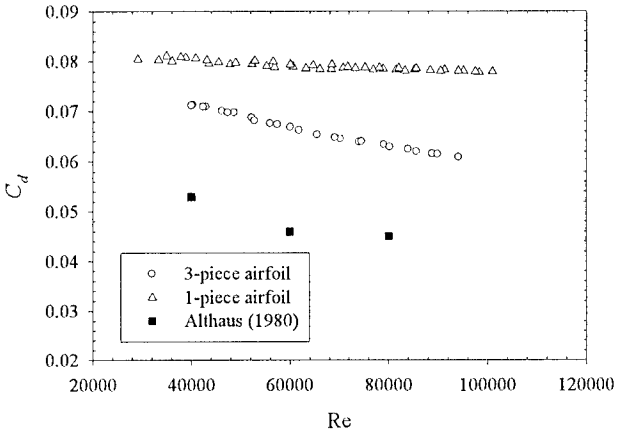

(b) Drag coefficient

Figure 72: Endplates effect on 2D characteristics of Eppler 61 airfoil at $\alpha = -2°$ with UND-FB2

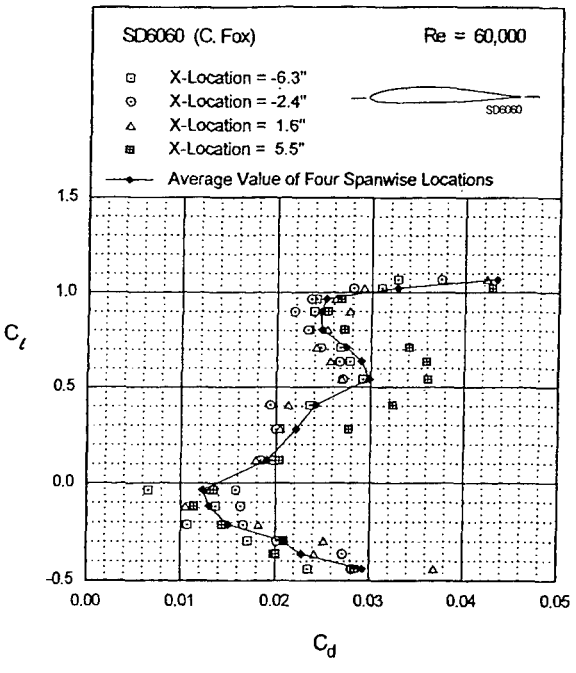

Figure 73: Drag polar for SD6060 airfoil at $Re_c = 60,000$ (Selig et al., 1995)

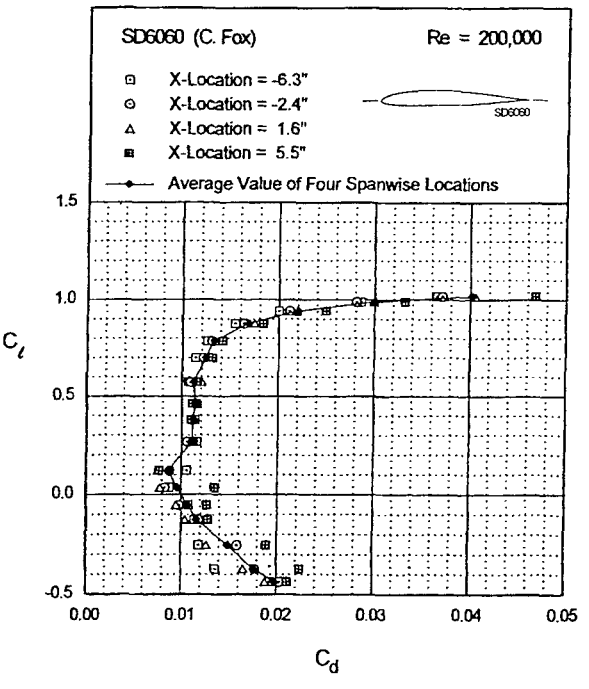

Figure 75: Drag polar for SD6060 airfoil at $Re_c = 200,000$ (Selig et al., 1995)

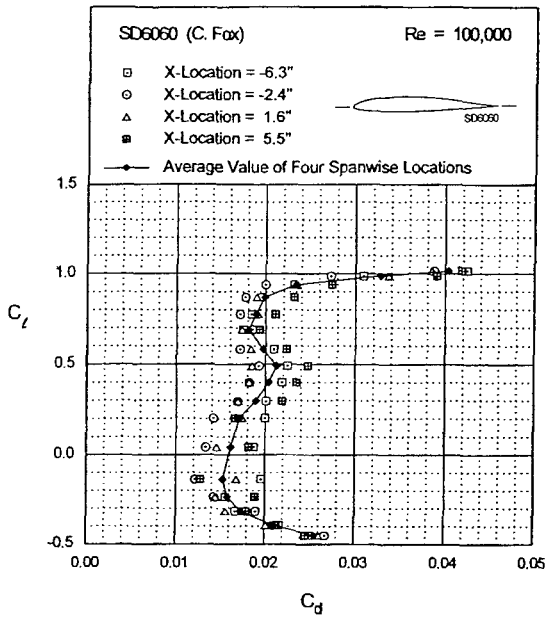

Figure 74: Drag polar for SD6060 airfoil at $Re_c = 100,000$ (Selig et al., 1995)

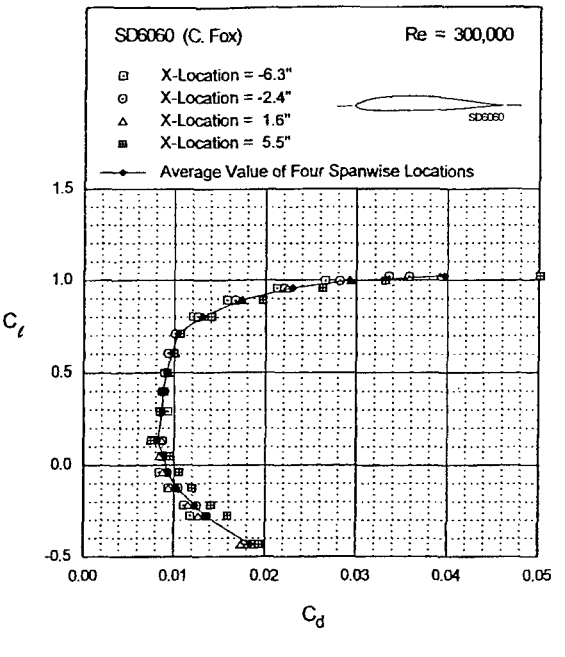

Figure 76: Drag polar for SD6060 airfoil at $Re_c = 300,000$ (Selig et al., 1995)

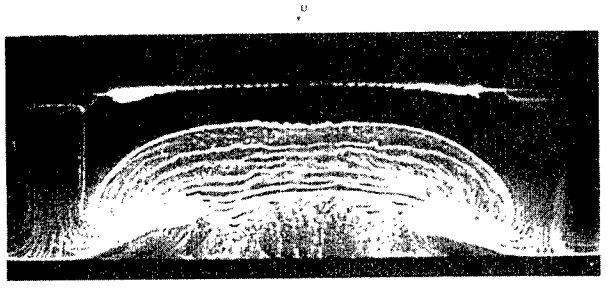

(a) Oil flow on Clark Y airfoil at $Re_c = 2.5 \times 10^5$ (Peake and Tobak, 1982)

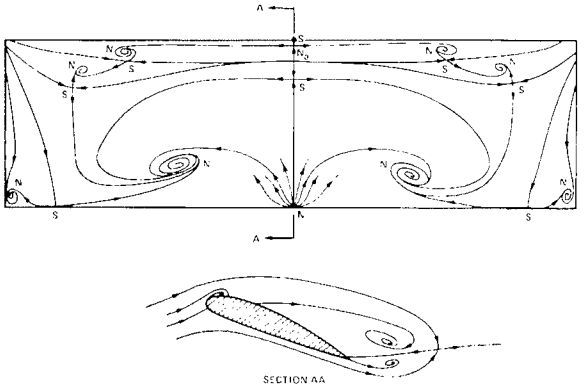

(b) Conjectures pattern of skin-friction lines (Peake and Tobak, 1982)

Figure 77: Flow pattern over a rectangular wing of aspect ratio 3.5 at angle of attack beyond stall

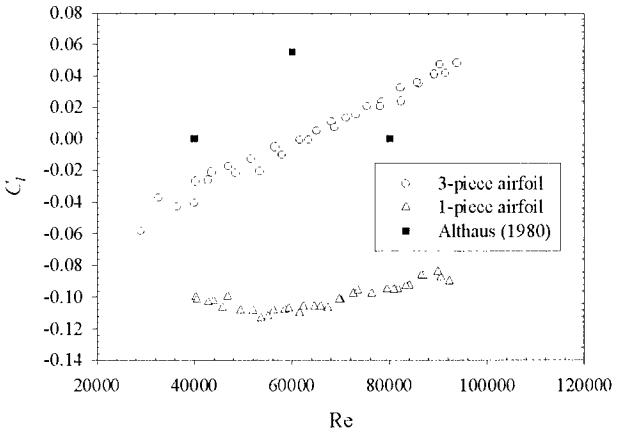

(a) Lift coefficient

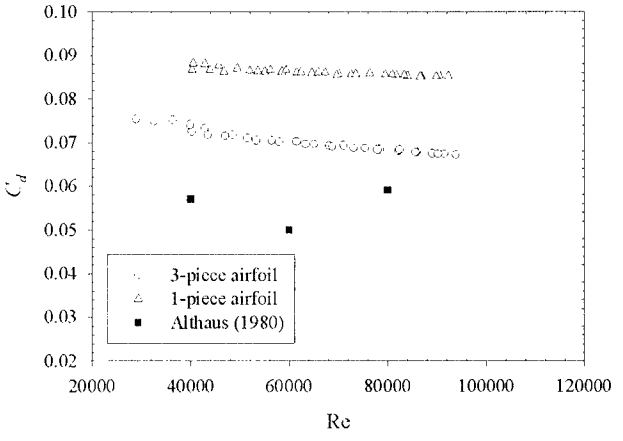

(b) Drag coefficient

Figure 78: Endplates effect on 2D characteristics of Eppler 61 airfoil at $\alpha = -2.5°$ with UND-FB2

For semi-infinite models, and also for finite models, the flow is highly three-dimensional, as was shown by Williams (1996) for low aspect-ratio wings at high angles of attack and Winkelman and Barlow (1980), whose work was reviewed by Peake and Tobak (1982). Figure 77 shows the flow pattern over a finite rectangular wing at an angle of attack beyond stall.

Other results for the 3-piece Eppler 61 model indicated that the zero-lift angle of attack was close to $-2.5°$ instead of $\alpha = -2°$, so tests were conducted at the new zero-lift angle of attack, as shown in Figure 78.

For the full model, it was determined that $(L/D)_{\max}$ occurred at $\alpha \approx 8°$. The 3-piece model was then tested at an angle of attack of $8°$. Unfortunately, the lift force acting on the middle section of the model became large enough at larger Reynolds numbers to deflect the lower tip of the section, which resulted in a poor alignment with the fixed bottom part of the model. Some three-dimensional effects were then believed to be created, which yielded results that did not follow a two-dimensional trend: the lift coefficient started to decrease with increasing Reynolds number. It is known that a semi-infinite model, where the bottom endplate has been removed, will have a lower lift coefficient than an infinite model, or pseudo-infinite model. Figure 79 shows the results at $\alpha = 8°$. It is interesting to note the significant increase in C_l just before $Re_c = 60,000$. This larger lift coefficient at Reynolds numbers greater than 60,000 was mentioned earlier when looking at the behavior of C_l with angle of attack for different Reynolds numbers.

Conclusions

It has been shown that sensitive equipment must be used to perform aerodynamic measurements on small models at very low Reynolds numbers. To achieve this goal, a new platform aerodynamic balance was designed

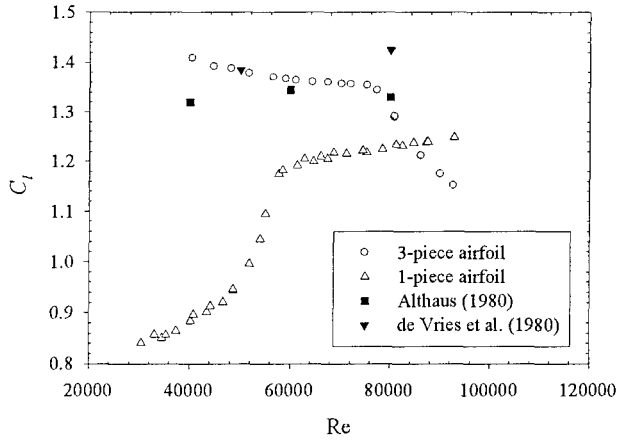

(a) Lift coefficient

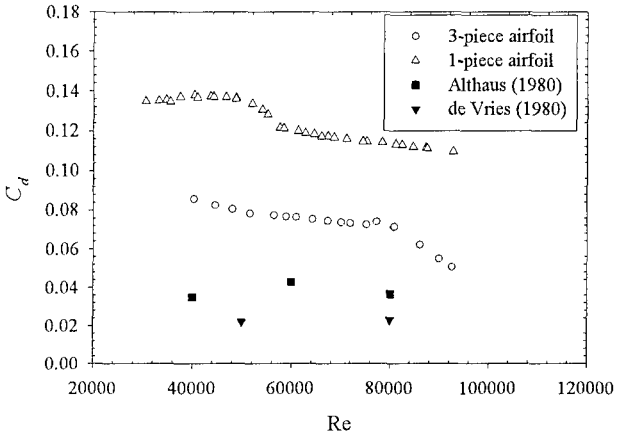

(b) Drag coefficient

Figure 79: Endplates effect on 2D characteristics of Eppler 61 airfoil at $\alpha = 8°$ with UND-FB2

and built at the University of Notre Dame. The balance shows good sensitivity, repeatability and accuracy. Techniques to reduce noise and increase the accuracy of the results in the water tunnel below Reynolds numbers of $40,000$ are still being investigated.

Moreover, it has been shown that cambered-plate wings with 4% camber offer better aerodynamic characteristics than flat-plate wings for a given Reynolds number. Reducing the Reynolds number can lead to poor performance due to the large reduction in $\left(\frac{L}{D}\right)_{\max}$ and $\left(\frac{C_L^{3/2}}{C_D}\right)_{\max}$ for both flat- and cambered-plate wings.

The turbulence intensity in the tunnel and the trailing-edge geometry have been shown to have a very small effect on the measurements of lift, drag and pitching moment on the thin models tested in this investigation. However, the presence of endplates can affect the results for lift and drag due to the interaction between the boundary layer growing on the endplate and the flow around the wing. The presence of endplates at low Reynolds numbers reduces the 2D lift and increases the 2D drag that would normally be obtained with a truly infinite model, according to tests on the Eppler 61 airfoil. Furthermore, for a given model, adding one endplate leads to an increase in lift compared to the case without an endplate. Testing finite wing models without endplates appears to be desirable at low Reynolds numbers because it eliminates endplate effects. The full effect of the endplates is still under investigation, especially for cambered-plate wings.

Finally, trends of $C_{D_{\min}}$ versus Re_c should be investigated by fixing the wing at the angle of attack yielding $C_{D_{\min}}$ and then varying the wind velocity, hence the Reynolds number, in the tunnel. This seems to help to eliminate scatter in the results. Tests using this technique on various flat plates have indicated the expected trends of a reduction in $C_{D_{\min}}$ and an increase in C_L with an increase in Reynolds number.

Acknowledgements

This research was sponsored by the U.S. Navy, Naval Research Laboratory, Washington, D.C. under Contract No. N00173-98-C-2025 and the Roth-Gibson Endowment at the University of Notre Dame. The author would like to thank Alain Pelletier for his effort and expertise in the experimental phase of this study as well as his help in preparing this manuscript. Special thanks go to Matthew Keennon of *AeroVironment*, William Davis, Jr. of *The Lincoln Laboratory*, Jeffrey Harris of *Sanders, A Lockheed Martin Company*, and Kevin Ailinger of the *Naval Research Laboratory* for sharing the results of their MAV development projects. Permission by Michael Selig to used his wake rake data and *The Lincoln Laboratory* for Figure 2 is gratefully acknowledged. The author would also like to thank Bruce Carmichael and James DeLaurier for their helpful comments on this manuscript.

References

Ailinger, K. G. "U.S. Navy Micro Air Vehicle Development." Unmanned Air Vehicle Systems Fourteenth International Conference, April 1999: 36-1–36-7.

Althaus, Dieter. *Profilpolaren für den Modellflug.* Neckar-Verlag, Institut für Aerodynamik und Gasdynamik, University of Stuttgart, 1980.

Anderson, John D., Jr. *Fundamentals of Aerodynamics.* 2nd ed. New York: McGraw-Hill, 1991.

Ashley, S. "Palm-Size Spy Planes." *Mechanical Engineering*, February 1998: 74-78.

Barber, T. J. "An Investigation of Strut-Wall Intersection Losses." *Journal of Aircraft,* Vol. 15, No. 10, October 1978: 676-681.

Bastedo, W. G. Jr., and T. J. Mueller. "The Spanwise Variation of Laminar Separation Bubbles on Finite Wings at Low Reynolds Numbers." AIAA Paper #85-1590, July 1985.

Batill, Stephen M., and Thomas J. Mueller. "Visualization of the Laminar-Turbulent Transition in the Flow Over an Airfoil Using the Smoke-Wire technique." AIAA Paper #80-0421, March 1980.

Brendel, Michael, and Arthur F. Huber II. "An Experimental Investigation of Flow Quality in an Indraft Subsonic Wind Tunnel Using a Single Hot Wire Anemometer." University of Notre Dame, November 1984.

Brooks, Gregory *Air Force Research Laboratory*, Private Communication, June 1999.

Burns, Thomas F. "Experimental Studies of Eppler 61 and Pfenninger 048 Airfoils at Low Reynolds Numbers." Master's Thesis, The University of Notre Dame, January 1981.

Carmichael, B. H. "Low Reynolds Number Airfoil Survey." Volume I, NASA Contractor Report 165803, November 1981.

Davis, W. R., Jr., B. B. Kosicki, D. M. Boroson, and D. F. Kostishack. "Micro Air Vehicles for Optical Surveillance." *The Lincoln Laboratory Journal*, Vol. 9, No. 2, 1996: 197-213.

Davis, W. R., Jr. *The Lincoln Laboratory*, Private Communication, June 1999.

de Vries, J., G. H. Hegen, and L. M. M. Boermans. "Preliminary Results of Windtunnel Measurements at Low Reynolds Numbers on Airfoil Section E61." Intern Report LSW 80-5, 1980.

Dornheim, M. A. "Unmanned Aerial Vehicles: Tiny Drones May Be Soldiers' New Tool." *Aviation Week & Space Technology*, June 8, 1998: 42-48.

Eidetics®. *Operations Manual: Flow Visualization Water Tunnel.*

Fulghum, D. A. "Miniature Air Vehicles Fly Into Army's Future." *Aviation Week & Space Technology*, November 9, 1998: 37-38.

Harris, J. D. *Sanders, A Lockheed Martin Company,* Private Communication, 1999.

Hawthorne, W. R. "The Secondary Flow About Struts and Airfoils." *Journal of the Aeronautical Sciences*, Vol. 21, No. 1, January 1954: 588-608.

Huber, Arthur F., II. "The Effects of Roughness on an Airfoil at Low Reynolds Numbers." Master's Thesis, The University of Notre Dame, May 1985.

Jackson, Paul, ed. *Jane's All the World's Aircraft.* Jane's Information Group, 1996-97.

Keennon, M. *AeroVironment*, Private Communication, June 1999.

Kline, S. J., and F. A. McClintock. "Describing Uncertainties in Single-Sample Experiments." *Mechanical Engineering*, Vol. 75, No. 1, January 1953: 3-8.

Laitone, E. V. "Aerodynamic Lift at Reynolds Numbers Below 7×10^4." *AIAA Journal,* Vol. 34, No. 9, September 1996: 1941-1942.

Laitone, E. V. "Wind Tunnel Tests of Wings at Reynolds Numbers Below 70,000." *Experiments in Fluids,* Vol. 23, 1997: 405-409.

McMasters, J. H., and M. L. Henderson. "Low Speed Single Element Airfoil Synthesis." *Tech. Soaring,* Vol. 2, No. 2, 1980: 1-21.

Miley, S. J. "An Analysis of the Design of Airfoil Sections for Low Reynolds Numbers." Ph.D. Dissertation, Mississippi State University, 1972.

Morris, S. J. "Design and Flight Test Results for Micro-Signed Fixed-Wing and VTOL Aircraft." 1st International Conference on Emerging Technologies for Micro Air Vehicles, Georgia Institute of Technology, Atlanta Georgia, February 1997: 117-131.

Mraz, S. J. "Honey I Shrunk the Plane." *Machine Design*, October 1998: 35-42.

Mueller, T. J., and T. F. Burns. "Experimental Studies of the Eppler 61 Airfoil at Low Reynolds Numbers." AIAA Paper #82-0345, January 1982.

Mueller, T. J., and B. J. Jansen, Jr. "Aerodynamic Measurements at Low Reynolds Numbers." AIAA Paper #82-0598, March 1982.

Mueller, T. J., L. J Pohlen, P. E. Conigliaro, and B. J. Hansen, Jr. "The Influence of Free-Stream Disturbances on Low Reynolds Number Airfoil Experiments." *Experiments in Fluids.* Vol. 1, 1983: 3-14.

O'Meara, M. M., and T. J. Mueller. "Laminar Separation Bubble Characteristics on an Airfoil at Low Reynolds Numbers." *AIAA Journal,* Vol. 25, No. 8, August 1987: 1033-1041.

Pankhurst, R. C., and D. W. Holder. *Wind-Tunnel Technique.* London: Sir Isaac Pitman & Sons, 1952.

Peake, David J., and Murray Tobak. "Three-Dimensional Flows About Simple Components at Angle of Attack." AGARD Lecture Series No. 121 on High Angle-of-Attack Aerodynamics, Paper No. 2, 1982.

Pelletier, Alain. "A Study of the Nonlinear Aerodynamic Characteristics of a Slender Double-Delta Wing in Roll." Ph.D. Dissertation, The University of Notre Dame, April 1998.

Pohlen, Lawrence. "Experimental Studies of the Effect of Boundary Layer Transition on the Performance of the Miley (M06-13-128) Airfoil at Low Reynolds Numbers." Master's Thesis, The University of Notre Dame, January 1983.

Prazak, M. W., and T. J. Mueller. "Experimental Studies of an Eppler 61 Wing at Chord Reynolds Numbers from 12,000 to 63,000." Technical Note UNDAS-TN-256-1, July 1997.

Rae, William H. Jr., and Alan Pope. *Low-Speed Wind Tunnel Testing.* 2nd ed. New York: John Wiley & Sons, 1984.

Schlichting, Hermann. *Boundary-Layer Theory.* 7th ed. New York: McGraw-Hill, 1979.

Selig, Michael S., et al. *Summary of Low-Speed Airfoil Data.* Volume 1, Virginia: SoarTech Publications, 1995.

Strang, W. Z., R. F. Tomaro, and M. J. Grismer. "The Defining Methods of Cobalt60: A Parallel, Implicit, Unstructured Euler/Navier-Stokes Flow Solver." AIAA Paper #99-0786, January 1999.

Taylor, John W.R., ed. *Jane's All the World's Aircraft.* Jane's Information Group, 1969-70.

Tennekes, Henk. *The Simple Science of Flight: From Insects to Jumbo Jets.* Cambridge: The MIT Press, 1996.

Williams, David L., III. "Dynamic, Lateral Behavior of Low-Aspect-Ratio, Rectangular Wings at High Angles of Attack." Ph.D. Dissertation, The University of Notre Dame, April 1996.

Wilson, J. R. "Mini Technologies for Major Impact." *Aerospace America*, May 1998: 36-42.

Winkelmann, A. E., and J. B. Barlow. "Flowfield Model for a Rectangular Planform Wing Beyond Stall." *AIAA Journal,* Vol. 18, No. 8, August 1980: 1006-1008.